Biological Cybernetics (2023) 117:143–162
https://doi.org/10.1007/s00422-023-00962-z

Biological Cybernetics

ORIGINAL ARTICLE

Structure and dynamics that specialize neurons for high-frequency coincidence detection in the barn owl nucleus laminaris

Ben Drucker[1,2] · **Joshua H. Goldwyn**[1]

Received: 8 September 2022 / Accepted: 14 March 2023 / Published online: 2 May 2023

Abstract

A principal cue for sound source localization is the difference in arrival times of sounds at an animal's two ears (interaural time difference, ITD). Neurons that process ITDs are specialized to compare the timing of inputs with submillisecond precision. In the barn owl, ITD processing begins in the nucleus laminaris (NL) region of the auditory brain stem. Remarkably, NL neurons are sensitive to ITDs in high-frequency sounds (kilohertz-range). This contrasts with ITD-based sound localization in analogous regions in mammals where ITD sensitivity is typically restricted to lower-frequency sounds. Guided by previous experiments and modeling studies of tone-evoked responses of NL neurons, we propose NL neurons achieve high-frequency ITD sensitivity if they respond selectively to the small-amplitude, high-frequency oscillations in their inputs, and remain relatively non-responsive to mean input level. We use a biophysically based model to study the effects of soma–axon coupling on dynamics and function in NL neurons. First, we show that electrical separation of the soma from the axon region in the neuron enhances high-frequency ITD sensitivity. This soma–axon coupling configuration promotes linear subthreshold dynamics and rapid spike initiation, making the model more responsive to input oscillations, rather than mean input level. Second, we provide new evidence for the essential role of phasic dynamics for high-frequency neural coincidence detection. Transforming our model to the phasic firing mode further tunes the model to respond selectively to the oscillating inputs that carry ITD information. Similar structural and dynamical mechanisms specialize mammalian auditory brain stem neurons for ITD sensitivity, and thus, our work identifies common principles of ITD processing and neural coincidence detection across species and for sounds at widely different frequencies.

Keywords Sound localization · Coincidence detection · Neural dynamics · Soma–axon coupling · Phasic spiking

1 Introduction

A principal cue for sound source localization is the difference in arrival times of sounds at an animal's two ears (interaural time difference, ITD). ITDs depend on animals' head sizes and are small compared to typical neural timescales. The maximum ITD, for sounds arriving from one side, is approximately 800 μs in humans (Tollin and Yin 2009) and approximately 250 μs to 300 μs in barn owls (accounting for ruff feathers, von Campenhausen and Wagner 2006). Neurons and neural circuits that process ITDs are specialized for temporal precision so that they can compare the timing of inputs at this submillisecond scale (Grothe et al. 2010, 2018). Binaural ITD processing begins in mammals in the medial superior olive (MSO) and in birds in the nucleus laminaris (NL). Neurons in these two nuclei are often characterized as coincidence detectors because they respond with higher firing rates when brief inputs arrive nearly simultaneously (Goldberg and Brown 1969; Sullivan and Konishi 1986; Carr and Konishi 1990; Yin and Chan 1990; Reyes et al 1996; Batra et al. 1997; Svirskis et al. 2004; Franken et al. 2015) and because they have been considered as possible neural substrates for Jeffress's influential theory of sound source localization by delay lines (Jeffress 1948; Carr and Konishi 1988).

Communicated by Benjamin Lindner.

✉ Joshua H. Goldwyn
jhgoldwyn@gmail.com

Ben Drucker
ben.drucker@icloud.com

[1] Department of Mathematics and Statistics, Swarthmore College, 500 College Ave, Swarthmore, PA 19081, USA

[2] Pacific Northwest National Laboratory, 902 Battelle Blvd, Richland, WA 10587, USA

Although MSO and NL neurons share a similar role in auditory processing, they can operate at widely different frequency ranges in some species. ITD-sensitive MSO neurons are thought to primarily aid in the localization of low-frequency sounds due to the limits of phase locking of their inputs (Joris et al. 1994) and consistent with the classical duplex theory of sound localization (Rayleigh 1907). NL neurons in barn owls, in contrast, operate on much higher-frequency sounds. Barn owls accurately localize sounds in the 4 kHz to 8 kHz range (Knudsen and Konishi 1979) and NL neurons shows ITD sensitivity in this frequency range as well (Carr and Konishi 1990; Funabiki et al. 2011).

Extracting ITDs from kilohertz-scale signals poses a difficult computational challenge for coincidence detector neurons. At these high frequencies, inputs to NL neurons are not resolved as isolated synaptic events whose relative timing can be compared. Instead, sound-evoked voltage responses in the soma of NL neurons appear as small-amplitude oscillations at the frequency of the tone input, termed the sound analogue potential (SAP) (Funabiki et al. 2011). Essential features of the SAP described by Funabiki and colleagues are (1) SAP amplitude varies with ITD, but the mean SAP level does not; and (2) NL firing rate increases with increases in SAP amplitude, but does not depend on SAP mean. These observations suggest that high-frequency ITD processing in the barn owl requires that NL neurons respond to the amplitude of high-frequency oscillating inputs (SAP amplitude) while remaining insensitive to slower changes in the baseline input level (SAP mean).

Figure 1 summarizes our approach. Synaptic conductances exhibiting high-frequency sinusoidal oscillations drive activity of a two-compartment NL neuron model (Fig. 1A). The NL model is biophysically based (Hodgkin–Huxley style) and is based on a model that has been applied to in vivo data (Ashida et al. 2007; Funabiki et al. 2011). Membrane conductance in each compartment control the local leak currents in each compartment (I_1 and I_2 in the schematic). An axial conductance parameter controls the current flow between the two compartments (I_{ax}). We adapt the model by varying the strength of these currents in a principled manner to explore how soma–axon coupling affects spiking dynamics and ITD sensitivity. The synaptic conductance signal that NL neurons receive is the sum of two high-frequency sinusoidal oscillations. Coincident inputs (ITD $=$ 0 μs) produce larger-amplitude oscillations than non-coincident inputs (Fig. 1B). NL neurons must respond selectively to the amplitude of high-frequency oscillations to extract ITD information from their inputs.

We show that electrical separation of the soma and the axon improves neural coincidence detection. When the soma and axon regions are weakly coupled, spike generation in the NL neuron model depends less on the baseline level of the input than in the case of strong coupling between soma and axon. We identify two dynamical features associated with weak soma–axon coupling that benefit high-frequency neural coincidence detection: linear subthreshold dynamics (as opposed to amplified, supralinear responses to subthreshold inputs) and rapid spike initiation. The importance of electrical separation between soma and axon regions for high-frequency ITD processing accords with related studies of NL neurons (Kuba et al. 2006; Ashida et al. 2007) (and similar work in MSO neurons (Lehnert et al. 2014; Goldwyn et al. 2019)), but we offer novel and clarifying insights into how structure (soma–axon coupling) affects dynamics and enhances ITD encoding by coincidence detection.

A feature of phasic neurons (also known as Type III excitability) is that noise variance (fluctuation amplitude) can drive spiking activity (Lundstrom et al. 2008, 2009; Gai et al. 2010; Huguet et al. 2017). In contrast, phasic neurons do not fire repetitively to constant intensity or slowly varying inputs (such as long duration current pulses) (Meng et al. 2012). NL neurons exhibit phasic firing in vitro (Reyes et al 1996), but biophysically based models developed previously for NL neurons are tonic (produce repetitive spiking in response to sufficiently strong constant inputs) (Ashida et al. 2007; Funabiki et al. 2011). We hypothesized that if NL neurons operated in the phasic mode, then synaptic inputs in the form of high-frequency oscillations could drive spiking activity that is selective for oscillation amplitude in a manner similar to how variance of noisy inputs drives spiking activity in phasic neurons. Indeed, we show that transforming our model to the phasic firing tunes the model to respond selectively to the small-amplitude, high-frequency signals that carry ITD information. This finding is consistent with the general theory of fluctuation sensitivity in phasic neurons and here we add to the understanding of the functional significance of phasic dynamics for high-frequency inputs. In sum, our work points to coherent principles of soma–axon coupling configurations and spiking dynamics that specialize auditory neurons for coincidence detection across species and for sounds at widely different frequency scales.

2 Results

2.1 Time difference sensitivity is greater for weakly coupled soma and axon regions

To study neural coincidence detection and ITD sensitivity in the barn owl NL, we constructed a two-compartment model with parameters adapted from an established model of these neurons (Funabiki et al. 2011). The two compartments represent a soma-dendritic region (compartment 1) and an axonal region of spike generation (compartment 2). Synaptic inputs target the first compartment and spike-generating sodium currents are restricted to the second compartment

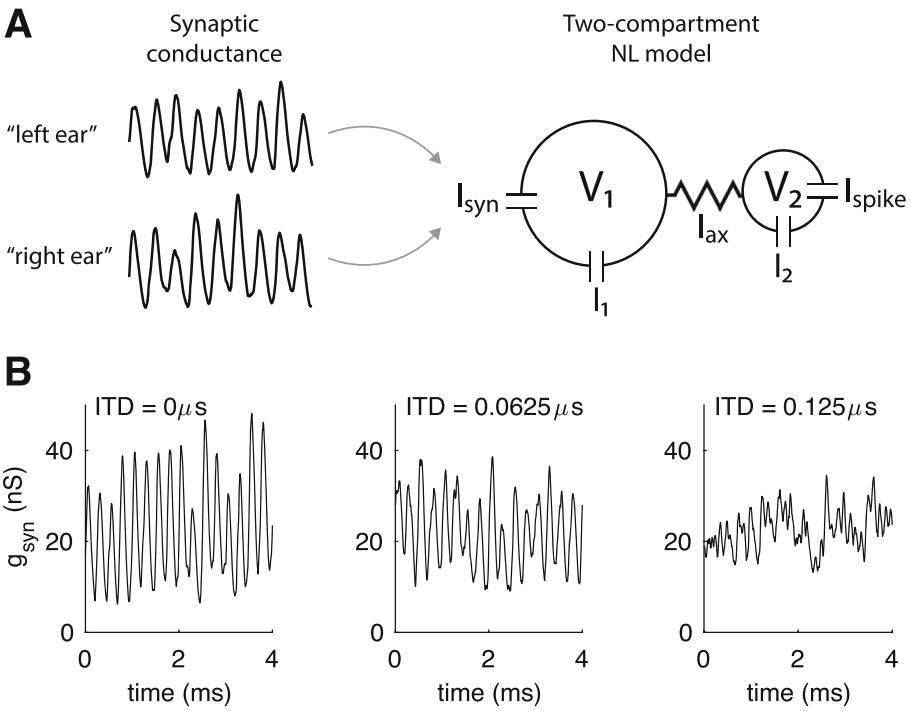

Fig. 1 Schematic of modeling approach with example synaptic inputs. **A** Synaptic conductance are generated, one for each "ear," with a possible time delay between the two signals to represent interaural time difference (ITD). The sum of the two synaptic conductance streams drives activity in a two-compartment model of NL neuron. **B** The summed "two ear" synaptic conductance exhibits a sinusoidal oscillation at the input frequency (4 kHz in these examples). Oscillation amplitude decreases as ITD increases. ITD sensitivity in NL neurons requires they respond selectively to the oscillation amplitude of their high-frequency inputs

with dynamics described by Hodgkin–Huxley-type nonlinear differential equations. All dynamic features of the model are the same as in the work of Funabiki and colleagues (synaptic model, membrane time constant in the soma, kinetics of voltage-gated conductances).

We modified the model by varying total conductance in the two compartments and axial conductance connecting the two regions and, in parallel, adjusting sodium conductance to maintain consistent excitability. We did this in a systematic manner, by identifying forward coupling strength ($\kappa_{1\to2}$) and backward coupling strength ($\kappa_{2\to1}$) parameters according to the method in Goldwyn et al. (2019) (and see Methods for further details). These coupling constants can also be understood as the attenuation ratios of steady-state voltages. The rationale for this parameter exploration is that spikes in NL neurons are thought to be primarily generated in the axon initial segment (Ashida et al. 2007), but physiological measurements are typically made in the soma. Our method enables us to constrain soma dynamics by available physiological measurements, while giving us freedom to explore the effect of soma–axon coupling and axon physiology (spike shape, for instance) on NL dynamics and function. A more complete understanding of how soma–axon coupling and axonal dynamics are specialized for ITD sensitivity is of particular interest in the NL because physiology can vary across the NL (Kuba et al. 2006; Kuba 2012) and may be dynamically adjusted during development (axon initial segment plasticity, as in Kuba et al. 2014).

By construction, all models (regardless of coupling configuration) have nearly identical passive soma dynamics, but the addition of sodium current in the second compartment leads to marked difference in spiking dynamics. In particular, models with weak soma–axon coupling have large-amplitude, fast-initiating, "all-or-nothing" spikes (Fig. 2B) whereas spikes in strongly coupled models are more graded with more gradual upstrokes (Fig. 2D). To make consistent comparisons across coupling configurations, we separately determined maximal sodium conductance for each coupling configuration to achieve a fixed peak firing rate in simulated responses. Specifically, we generated two synaptic input streams (meant to represent 4 kHz tone-evoked responses from the two ears) with a possible time difference (ITD). For in-phase inputs (ITD= 0 ms), such as those shown in Fig. 2A1, we set maximum sodium conductance so that the average firing rate of the NL neuron model was 500 spikes per second. Importantly, when synaptic events were evoked by out-of-phase 4 kHz sine waves (ITD= 125 μs, as in the example in Fig. 2A2), there are clear differences in simulated

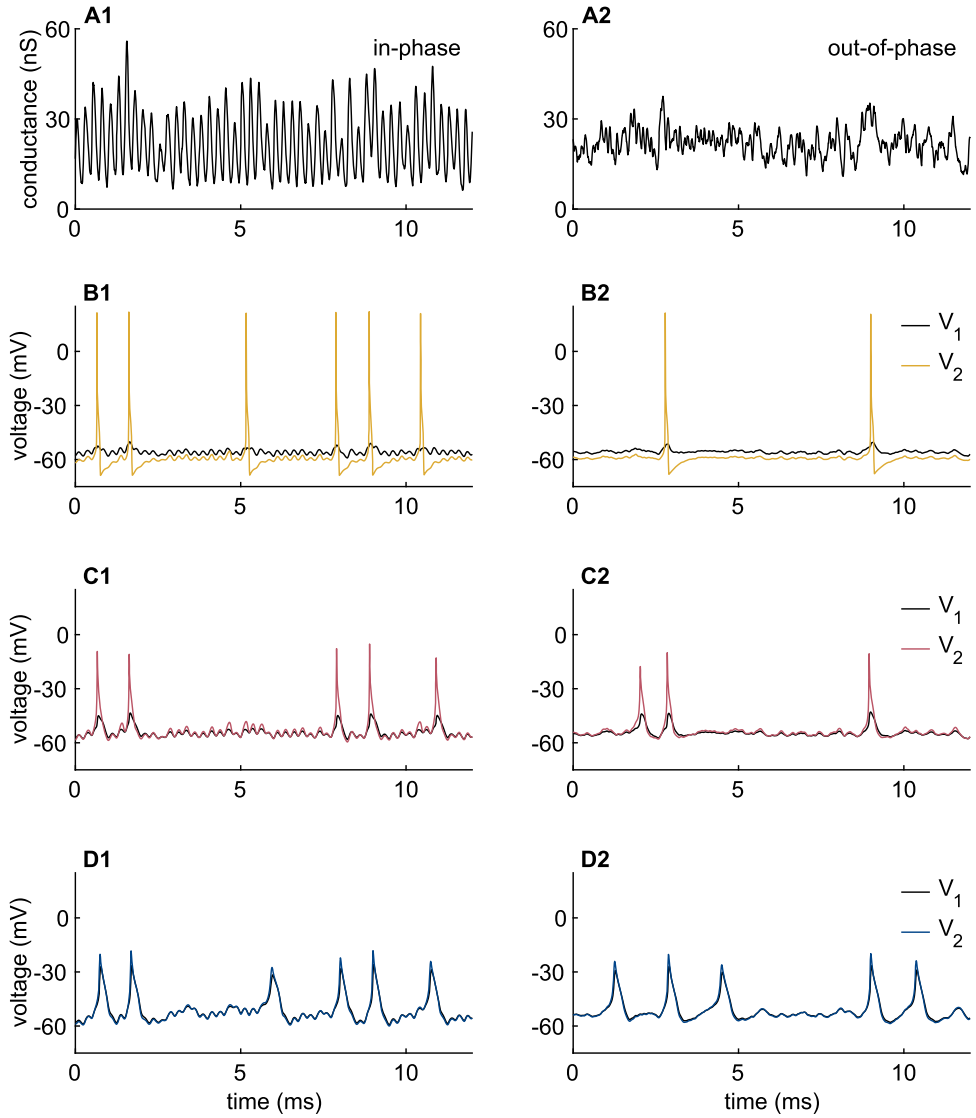

Fig. 2 Spiking dynamics of a two-compartment NL model. **A** Synaptic conductance time courses for 4 kHz in-phase (left column) and out-of-phase (right column) inputs. **B**–**D** Membrane voltage responses to inputs in **A**, using three different soma-to-axon coupling configurations: $(\kappa_{1\to2}, \kappa_{2\to1}) = (0.3, 0.2)$ in **B**, (0.9, 0.5) in **C** and (0.9, 0.9) in **D**. Gray curves in these panels show soma voltage (V_1) and colored curves show axon voltage (V_2)

NL firing rate. In these examples, the model with weaker coupling produces just two spikes (Fig. 2B2) (a decrease from the in-phase response). The model with stronger coupling produces five spikes in response to the same input (Fig. 2D2) which is nearly equal to its in-phase firing rate.

The coupling configuration $\kappa_{1\to2} = 0.9$ and $\kappa_{2\to1} = 0.5$ is similar to the previously developed model that is the starting point for our work (Funabiki et al. 2011). We show responses of this model in Fig. 2C. They used their model to make comparisons to in vivo recordings of NL responses to pure tones, so this parameter setting can be taken as a physiologically plausible coupling configuration. Other configurations are also possible due to natural variations across neurons and animals, or during different stages of development, among other reasons. Our modeling approach allows us to assess a range of possible coupling configurations in a systematic manner.

We next computed ITD tuning curves, by simulating neural responses to inputs with a range of time differences (Fig. 3A). For the strongly coupled model, in which V_1 and V_2 are nearly isopotential, firing rates do not vary substantially with ITD. This is evident in the relatively flat firing rate curve for the case of $\kappa_{1\to2} = \kappa_{2\to1} = 0.9$ (Fig. 3A1). The other coupling configurations produce larger differences in the firing rates evoked by in-phase inputs versus out-of-

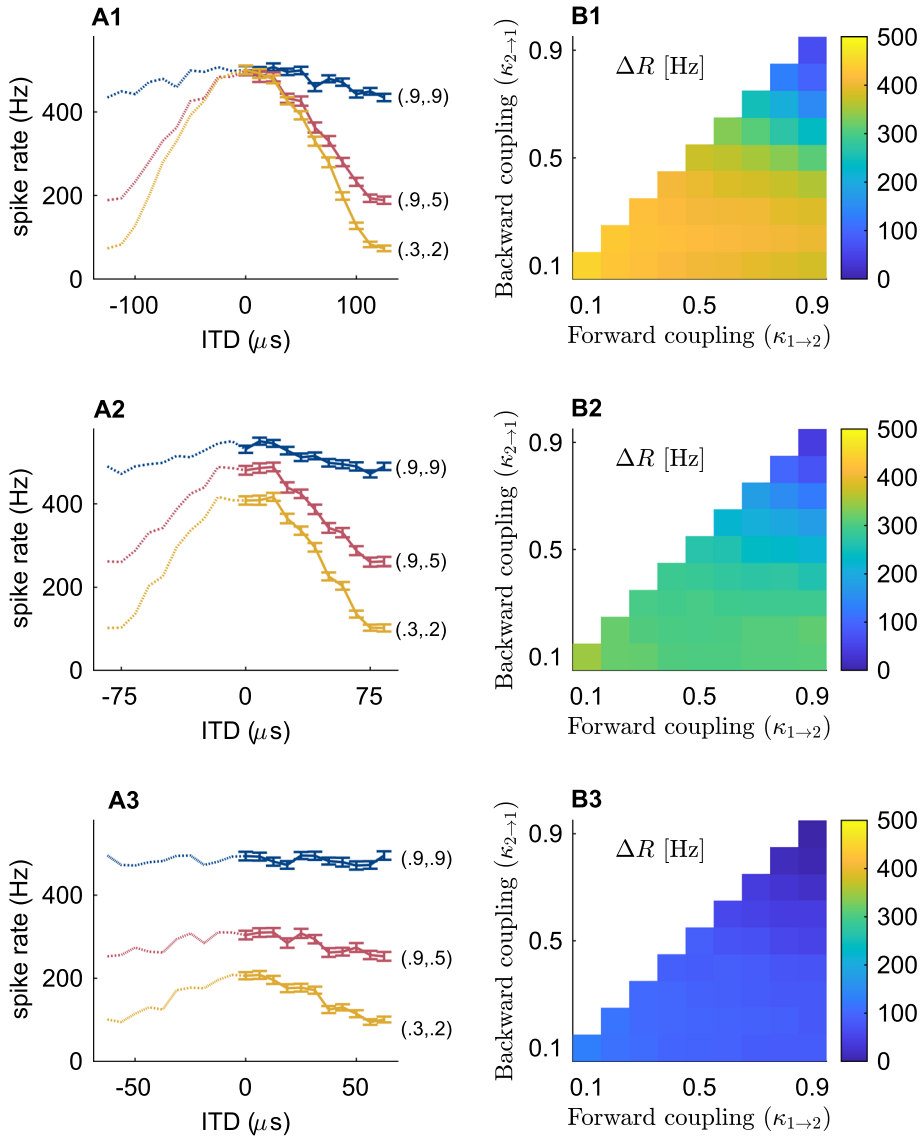

Fig. 3 Tuning to input time difference requires electrically isolated soma and axon compartments. Left column: ITD tuning curves (spike rate as function of input time difference) in response to 4 kHz (**A1**), 6 kHz (**A2**) and 8 kHz (**A3**) inputs. Coupling configurations and color scheme is same as Fig. 2. Dotted lines are a reflected version of computed values. Error bars represent standard error in the mean firing rate from 100 repeated simulations. Sodium conductance is determined so 500 spikes/sec is peak firing rate for all configurations. Right column: Difference between in-phase and out-of-phase firing rates across the space of coupling configurations (ΔR, scale bar at right) for 4 kHz (**B1**), 6 kHz (**B2**) and 8 kHz (**B3**) inputs. ΔR is smallest for strong coupling and increases for electrically isolated soma and axon compartments (weaker coupling)

phase inputs. This further confirmed that electrical separation of soma and axon improves ITD sensitivity.

To expand on these initial observations, we measured the difference between in-phase and out-of-phase firing rates across a full range of coupling configurations (Fig. 3B1). This measure of ITD tuning curve depth, which we denote by ΔR, is a commonly used measure of ITD sensitivity in simulation studies and recordings of NL neurons (Ashida et al. 2007; Funabiki et al. 2011; Grau-Serrat et al. 2003). By this measure, there is a relatively broad range of coupling configurations with large ΔR (good ITD sensitivity). The disadvantage of strong coupling is confined to a relatively small region of parameter space (small ΔR in the upper right corner).

ITD tuning depth decreases with higher input frequency (rows 2 and 3 in Fig. 3), although some ITD sensitivity remains for models with weak soma–axon coupling for input frequencies as high as 8 kHz (as evident in the ITD tuning curve for the $(\kappa_{1\to2}, \kappa_{2\to1}) = (0.3, 0.2)$ in Fig. 3A3). ITD tuning curves change with increasing input frequency in ways that differ depend on coupling configuration. The ITD tun-

ing curve for the strongly coupled model ($(\kappa_{1\to2}, \kappa_{2\to1}) = (0.9, 0.9)$) in Fig. 3A flattens because firing rates saturate at a high firing rate for all ITDs. In contrast, the ITD tuning curves for the models with weaker coupling in Fig. 3A flatten at higher input frequencies because the maximum firing rates in these models decrease with frequency. We can describe this distinction by drawing an analogy to signal detection theory. Supposing NL spikes are meant to signal the occurrence of coincident synaptic inputs, we can say the false positive rate increases in the strongly coupled model in response to higher input frequencies, whereas the true positive rate (sensitivity) decreases in more weakly coupled models.

In the following, we explain the advantage of weaker coupling configurations for ITD tuning by clarifying the signal processing imperative for NL neurons to respond to oscillation amplitude, not mean level, and by explaining how structure creates dynamics that support effective high-frequency ITD coding.

2.2 Coding imperative: ITD represented by oscillation amplitude

Informed by insightful experimental and theoretical work in the NL (Ashida et al. 2007, 2013a, b; Funabiki et al. 2011), we take the view that ITD information is delivered to NL neurons via the amplitude of oscillating synaptic inputs. These oscillations evoke the small-amplitude, high-frequency oscillations in the somatic membrane potential of NL neuron termed the sound analogue potential (SAP) (Funabiki et al. 2011). For NL neurons to effectively encode ITD signals, the input amplitudes should drive NL spiking activity, not the mean input level. An idealized view of this computation is NL neurons must monitor their synaptic inputs and use spike generation in the axon to signal when amplitudes of voltage oscillations in the soma exceed some threshold. Threshold crossings should be determined by amplitude and not mean input level.

We illustrate this coding perspective by computing, on a cycle-by-cycle basis, the mean and amplitude of the excitatory synaptic conductances that are inputs to the NL model. The period of each cycle is 250 μs, as dictated by our use of a 4 kHz input tone. A scatter plot of 100 cycles of synaptic inputs reveals, as expected, that in-phase synaptic inputs are more distinguishable from out-of-phase inputs by differences in amplitude, not the mean input level (Fig. 4A, see also Fig. 2A for example synaptic conductance time courses).

To explore further this idealized view of NL neurons as cycle-by-cycle observers of their inputs, we computed a classifier boundary defined using Fisher's linear discriminant (Bishop 2006). Synaptic inputs that fall above the boundary would be reported by an ideal observer of these synaptic conductances as in-phase inputs. The classifier boundary is upward sloping because oscillation amplitudes are positively correlated with mean input level for in-phase inputs. This suggests a stringent coding imperative for NL neurons: they should generate spikes when the amplitude of their high-frequency inputs are sufficiently large, and also, they should avoid generating spikes to inputs with large mean values.

This description of an NL neuron as a signal classifier observing its inputs is, of course, an over-simplification of the biophysical processes at work. We do not expect NL neurons to act exactly like such ideal observers because intrinsic dynamics of NL neurons (such as refractory periods) do not allow spike generation to occur on a cycle-by-cycle basis in response to high-frequency inputs. Nevertheless, this perspective gives a helpful framework for considering how characteristics of NL spike generation impact ITD sensitivity.

To relate this signal classification perspective to modeling results, we used sinusoidal conductance inputs (as opposed to the random synaptic inputs used in other simulations) to compute thresholds for repetitive firing as a function of input mean and amplitude (Fig. 4B). For all coupling configurations, the slope of these threshold curves was negative, indicating the model becomes more excitable for larger mean input levels. This is inconsistent with ideal observer's classification boundary (but we will see later, in Sec 2.5, that phasic dynamics can create positively sloped threshold curves). Among the coupling configurations tested in Fig. 4, the strongly coupled model had the steepest threshold curve. For g_{mean} larger than roughly 15 nS, changes in mean input level alone, not oscillation amplitude, can drive changes in firing rate for this coupling configuration. This parallels the ITD tuning results presented above (Fig. 3A) by showing that strong electrical coupling between soma and axon is disadvantageous for ITD tuning, when compared to configurations with electrically separated soma and axon compartments.

2.3 Distinctive dynamics of strongly coupled models that hinder high-frequency coincidence detection

What accounts for enhanced ITD tuning for models with stronger soma–axon coupling? We identified two dynamical features caused by strong coupling that distinguish those models from models with electrical isolation between soma and axon. These features are: (1) supralinear subthreshold integration in the soma and (2) slow spike initiation in the axon. By supralinear integration, we mean that the subthreshold current–voltage relation is nonlinear with positive concavity as in the $I-V$ curves shown in Fig. 5A. Amplification of subthreshold voltage is greatest for models with strong soma–axon coupling because strong soma-to-axon (forward) coupling activates sodium conductance, and in turn, strong axon-to-soma (backward) coupling enables axonal sodium current to depolarize the soma.

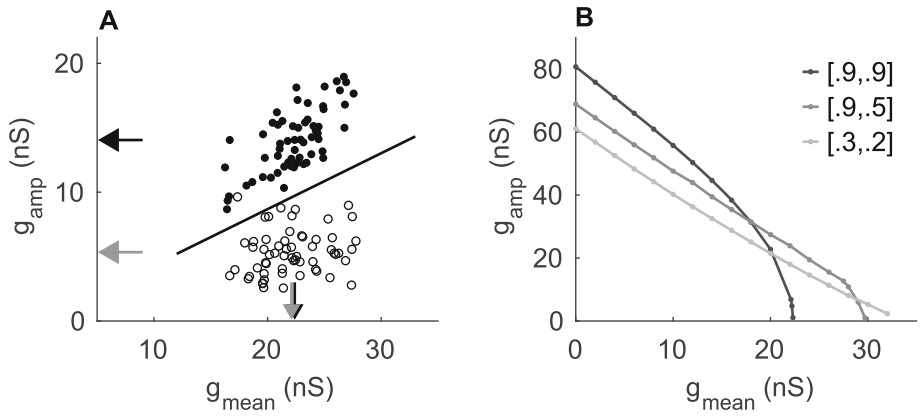

Fig. 4 High-frequency ITD processing requires sensitivity to cycle amplitude, not cycle mean, of high-frequency inputs. **A** Scatter plot of mean and amplitude of synaptic conductance measured relative to period of 4 kHz input frequency for in-phase inputs (filled circles) and out-of-phase inputs (empty circles). Arrow heads indicate mean values of these measures (black arrow for in-phase, gray for out-of-phase). A classification boundary based on Fisher's linear discriminant is indicated by the solid line. **B** Thresholds of repetitive firing in two-compartment NL model in response to sine-wave conductance. Coupling configurations and color scheme are same as Fig. 2

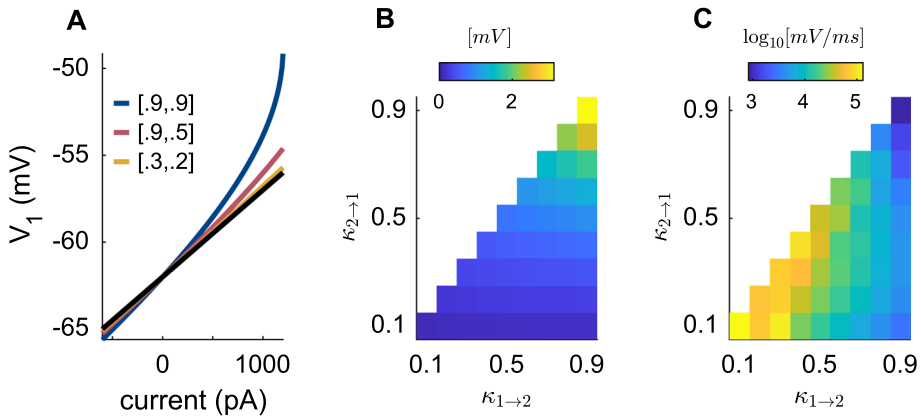

Fig. 5 Nonlinear mechanisms that distinguish strongly coupled models from models with electrically isolated compartments. **A** Steady-state soma voltage response to constant input current (I-V relation). Color code and coupling configurations are same as Fig. 2. Black line is response of the model g_{Na} removed (linear response with 5 $M\Omega$ soma input resistance). **B** Subthreshold V_1-amplification measured as the difference between steady-state V_1 responses to 1000 pA inputs for models with and without sodium current. **C** Maximum V_2 slope during spike upstrokes, calculated as average of 100 responses to in-phase inputs. Colors given on a logarithmic scale as indicated

We quantified the amount of amplification across the range of coupling configurations by calculating the steady-state V_1 (soma) voltage response to a subthreshold input (1000 pA constant current) and compared it to the V_1 value that would be expected for a purely passive model (recall that passive soma input resistance is fixed as a constant for all coupling configurations). The largest amplification occurs in models with strong soma–axon coupling, and models with weak soma–axon coupling have nearly linear $I-V$ relations (Fig. 5B).

In addition to affecting subthreshold integration, coupling configuration also changes the shape and dynamics of spikes (recall Fig. 3A, B). In strongly coupled models, voltage dynamics in the two compartments track one another closely. Spikes occur in both compartments with V_1 dynamics slowing the rate of upstroke. In weakly coupled models, by contrast, voltage dynamics in the axon are insulated from the soma. In these cases, fast activation of sodium current during a spike increases V_2 rapidly and without hindrance from the more slowly depolarizing soma.

We measured the maximum slope of spike upstroke in V_2 across coupling configurations (Fig. 5C). Spike upstrokes in weakly coupled models occur at rates that can be as much as one hundred times faster than the spikes in the most strongly coupled model. This finding is consistent with the previous modeling work showing that moving the location of a localized spike initiation zone to a position on the axon more distant from soma leads to a steeper spike upstrokes (Brette 2013). We are not aware of in vivo physiological measurements of spike shapes in NL axons.

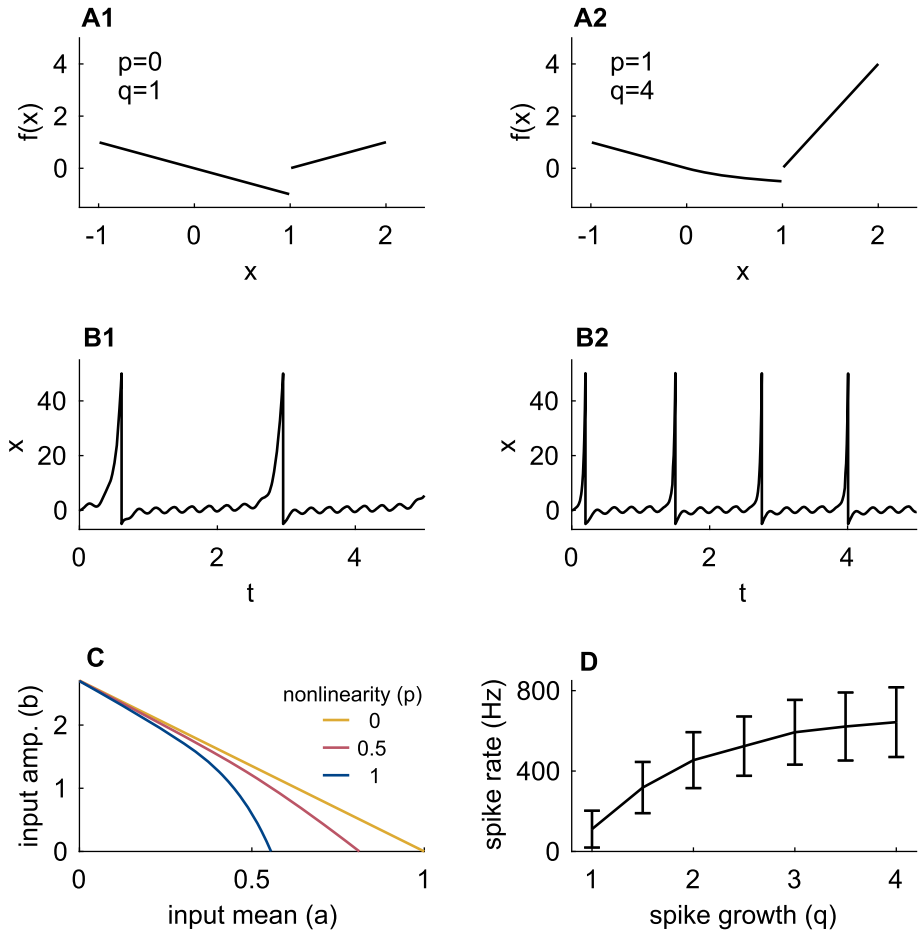

Fig. 6 Nonlinear integrate-and-fire model illustrates effects of subthreshold amplification and spike initiation speed on sensitivity to oscillation amplitude. **A** Piecewise defined function that governs model dynamics. An interpolation parameter (p) controls whether subthreshold integration is linear ($p = 0$ in **A1**) or supralinear ($p = 1$ in **A2**). A second parameter (q) controls the speed of spike initiation (the slope of $f(x)$ where $x > 1$). **B** Time courses of the dynamical variable $x(t)$ in response to 4 kHz sine-wave input, with parameter sets in B1 and B2 corresponding to those in **A1** and **A2**. Input current is zero mean ($a = 0$) and amplitude parameter is $b = 2.75$ (see Eq. 10). **C** Thresholds for repetitive firing in response to 4 kHz input with varying mean (ordinate) and amplitude (abscissa). The subthreshold nonlinearity p affects the slope of these threshold curves (as shown), but the spike slope q does not. **D** Mean spike rate in response to 4 kHz inputs with varying cycle amplitudes (with zero mean input) and linear subthreshold dynamics ($p = 1$). Error bars show standard deviations of 500 repeated trials

2.4 Advantages of linear subthreshold integration and fast spike initiation illustrated in an integrate-and-fire model

We hypothesized that the two dynamical features identified above that distinguish strongly coupled models from other coupling configuration (supralinear subthreshold integration and slow spike initiation) could account for degraded ITD sensitivity in models with strong soma–axon coupling. Our reasoning was as follows. Inputs to NL neurons are relatively weak—the SAP (soma voltage oscillation amplitude) is on the order of a few millivolts (Funabiki et al. 2011). Models of NL neurons must operate, therefore, near threshold so these small amplitudes suffice to evoke spiking in NL neurons (Ashida et al. 2007; Funabiki et al. 2011). At the same time, to maintain high-frequency ITD sensitivity, NL neurons must not respond to changes in input mean. Nonlinear amplification of subthreshold inputs is detrimental for high-frequency coincidence detection, therefore, because constant or slowly varying subthreshold inputs that are nonlinearly amplified can drive spiking activity even in the absence of oscillations related to meaningful ITD information. There is greater amplification of soma voltage in strongly coupled models than models with weak axon-to-soma coupling, so the strongly coupled configuration is not optimal for preventing spike initiation in response to constant or slowly varying inputs.

The second distinctive feature of strongly coupled models is (relatively) slow spike initiation. Fast spike initiation should be beneficial for high-frequency ITD detection.

The larger-amplitude portions of high-frequency oscillating inputs carry salient ITD information. When a portion of the high-frequency oscillating input has a large amplitude, due in part to random cycle-by-cycle variations in synaptic inputs), a rapidly initiated spike can be triggered before the input decreases (during the next phase of the input oscillation). Neurons with slowly initiating spikes, by contrast, may need to "integrate" over larger portions of their inputs before spikes fully develop. Neurons with gradual spike upstrokes would be less responsive to a randomly occurring oscillation with particularly large amplitude.

We illustrate how these two features affect high-frequency ITD detection using an integrate-and-fire model with (possibly) nonlinear subthreshold dynamics and exponential spike upstroke. An interpolation parameter p switches the model between linear subthreshold dynamics ($p = 0$) and supralinear subthreshold dynamics ($p = 1$). When the dynamical variable in the model exceeds a threshold level, the dynamics change to exponential growth. A gain parameter q controls the exponential rate of rise of x. When $x(t)$ exceeds the maximum value of $x_{\max} = 50$, the dynamical variable is returned to $x(t) = -5$, a reset condition typical for representing spikes in integrate-and-fire models. Figure 6A shows the graph of the piecewise function that governs the intrinsic dynamics of the model. A linear subthreshold model with slow spike initiation is shown in Fig. 6A1 ($p = 0, q = 1$) and a model with suprathreshold amplification and fast spike initiation is shown in Fig. 6A2 ($p = 1, q = 4$). Further details are given in Methods. We simulated responses of this model to high-frequency sinusoidal inputs, varying input mean (g_{mean}) and input amplitude (g_{amp}). Examples of spiking responses are shown in Fig. 6B with steeper spike upstroke visible in Fig. 6B2 due to the larger value of q in that simulations.

We have parametric control over subthreshold amplification and rate of spike initiation in this integrate-and-fire model. We first computed thresholds for repetitive spiking as a function of input mean and amplitude and found that increasing the degree of subthreshold amplification (increasing p) produces threshold curves that slope downward more steeply (Fig. 6C). This is qualitatively consistent with repetitive spiking threshold curve for the strongly coupled two-compartment model (Fig. 4B). In the simulations shown, we used $q = 3$ for the rate of spike growth in the integrate-and-fire model. In additional simulations (not shown), we varied q between 1 and 5 and observed no changes to these threshold curves.

Next, we varied the spike growth parameter q to confirm that rapid spike initiation increased sensitivity to high-frequency oscillation amplitude (Fig. 6D). For these simulations, we used inputs that were sinusoidal, but with oscillation amplitude that varied randomly on a cycle-by-cycle basis. Our rationale for this input structure was that most cycles would be subthreshold oscillations (by design) with some larger-amplitude oscillations occurring at random. Higher firing rates in response to this random input would indicate greater sensitivity to oscillation amplitude. We found, as expected, firing rates increased with the speed of spike initiation. The maximum upstroke speed in this model was roughly 500 ms^{-1} for $q = 1$ and increased to roughly 2000 ms^{-1} for $q = 4$. This values are comparable to the spike upstroke speeds in the two-compartment model (roughly 2.7 to 3.3 on the logarithmic scale, for reference to Fig. 5C). The results shown in Fig. 6D are for $p = 0$ (linear model), and we found qualitatively similar outcomes for models with nonlinear subthreshold dynamics ($p > 0$, results not shown).

2.5 Phasic dynamics enhance high-frequency ITD sensitivity

NL neurons display phasic dynamics in vitro (Reyes et al 1996) and phasic neurons are known to respond selectively to input variance (and not input mean) (Lundstrom et al. 2008, 2009; Meng et al. 2012). Previous models of NL neurons have not exhibited phasic firing (Ashida et al. 2007; Funabiki et al. 2011), so we were compelled to explore whether phasic dynamics would enhance high-frequency ITD sensitivity in the NL neuron model. We began by inspecting the dynamics of a reduced version of the model in which soma voltage V_1 is a (constant) input strength, sodium activation is set instantaneously to its voltage-dependent steady-state value $m_\infty(V_2)$ and g_{KHT} set to 0. These manipulations yielded a two-variable model (V_2−h) of axonal dynamics. The phase plane for this reduced axon model contains a fixed point that loses stability as it transitions from the left branch of the V_2-nullcline to the middle branch for sufficiently large input strength V_1 (Fig. 7A1). This transition is characteristic of tonic dynamics (Rinzel and Huguet 2013).

We found that a convenient way to convert this reduced, two-parameter, axon model to the phasic firing mode was to steepen the sodium inactivation function h_∞ by decreasing the parameter σ in Eq 7. The default value used in Fig. 7A1 and based on previous models (Funabiki et al. 2011) is $\sigma = 7.7$. When we steepened sodium inactivation by setting $\sigma = 5$, we found the fixed point remains stable and located on the left branch of the V_2-nullcline (Fig. 7A2). This indicates no possibility of repetitive firing to constant inputs (Meng et al. 2012).

We confirmed that these observations correctly generalized to the full two-compartment NL model by altering the steepness of the sodium inactivation curve in that model. We performed a two-parameter bifurcation analysis using input current strength I_0 and sodium conductance g_{Na} as bifurcation parameters (Fig. 7B). For the reference model using $\sigma = 7.7$, a region of tonic firing was present for sufficiently strong input current (gray shaded region in Fig. 7B1). Maximal sodium conductance for this configuration was

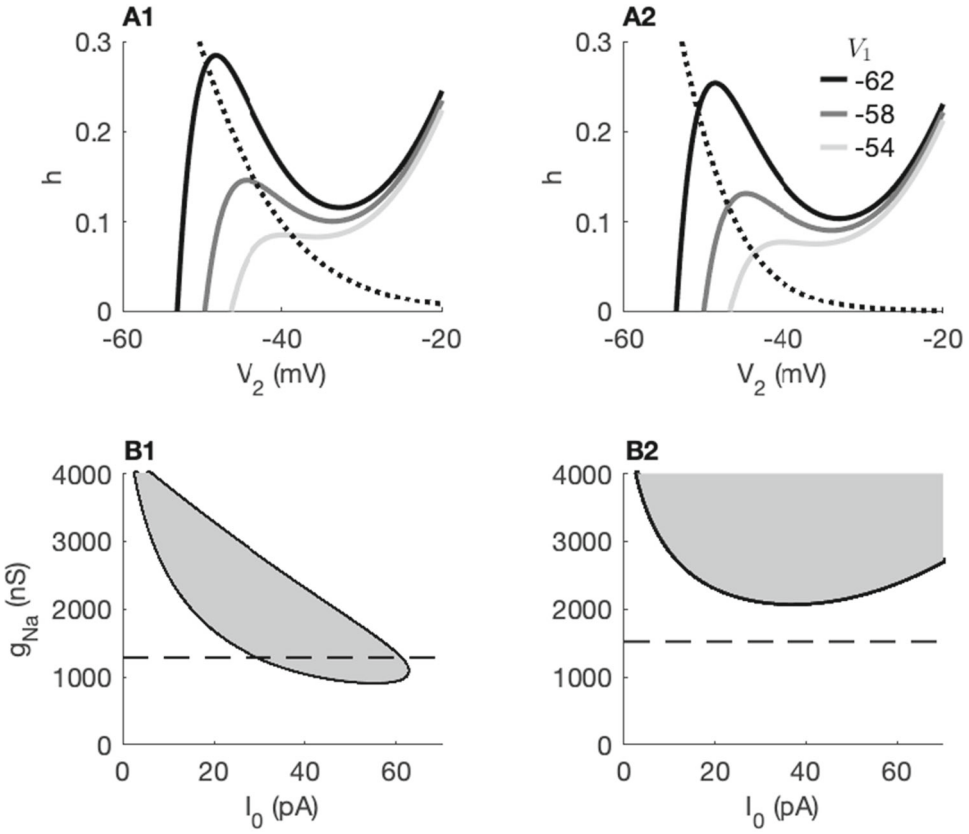

Fig. 7 Modification of sodium inactivation converts two-compartment model from tonic to phasic firing. Coupling configuration is $\kappa_{1\to 2} = 0.9, \kappa_{2\to 1} = 0.5$. **A** Phase plane diagrams for two-variable (reduced) axon model. Dotted line shows h-nullcline for the control model ($\sigma = 7.7$ in **A1**) and a model with steeper h_∞ function ($\sigma = 5$ in **A2**). Solid lines show V_2-nullclines for varying V_1 (treated as a constant, input parameter). **B** Two-parameter bifurcation study of two-compartment (full) NL model showing combinations of constant input current (I_0) and sodium conductance (g_{Na}) that produce tonic firing (shaded region) or phasic firing (non-shaded region). Horizontal dashed line marks the g_{Na} value used in ITD simulations (to satisfy criterion of 500 sp/s peak firing rate). Values of σ (steepness of h_∞) in **B1** and **B2** correspond to values in **A1** and **A2**, respectively

$g_{Na} = 1286$ nS (marked by dashed line that passes through the tonic firing region). This model fires repetitively for inputs with sufficiently large mean values. The model with steeper h_∞ and $g_{Na} = 1522$ nS does not fire repetitively to constant inputs, regardless of the input level (Fig. 7B2). Recall that g_{Na} is different in these two models because we selected g_{Na} separately for all model configurations to maintain the 500 sp/s firing rate at 0 μs ITD.

Converting the model from tonic to phasic firing substantially altered sensitivity to oscillation amplitude and improved ITD tuning. We first computed thresholds for repetitive firing to sinusoidal conductance (Fig. 8A). Earlier we observed these curves were downward sloping (Fig. 4B), even though an idealized signal classification view of this problem indicated that upward-sloped threshold curves would be optimal for coincidence detection (Fig. 4A). Reducing σ had the effect of flattening these threshold curves so that the model could be more sensitive to oscillation amplitude and less sensitive to input mean. In fact, at the smallest σ value tested (also a phasic model), portions of the threshold were upward-sloped and thus more similar to the ideal observer's classification boundary. Although we did not perform a detailed analysis of this upward-sloped portion of the threshold curve, this effect is consistent with our understanding of sodium inactivation as a mechanism for phasic firing. In particular, sustained depolarization caused by inputs with sufficiently large g_{mean} decreases the sodium inactivation variable h which, in turn, reduces the amount of sodium current available for spike initiation. For sufficiently a steep h_∞ curve (sufficiently small σ parameter), this decrease in h causes an overall decrease in excitability (evident as the upward-sloped portion of the spike threshold curve in Fig. 4A).

Consistent with these changes in responsiveness to sinusoidal conductance, we found that converting the model to phasic firing enhanced ITD tuning in the case of high-frequency simulated synaptic inputs (Fig. 8B). Visible changes to ITD tuning curves for smaller σ include both nar-

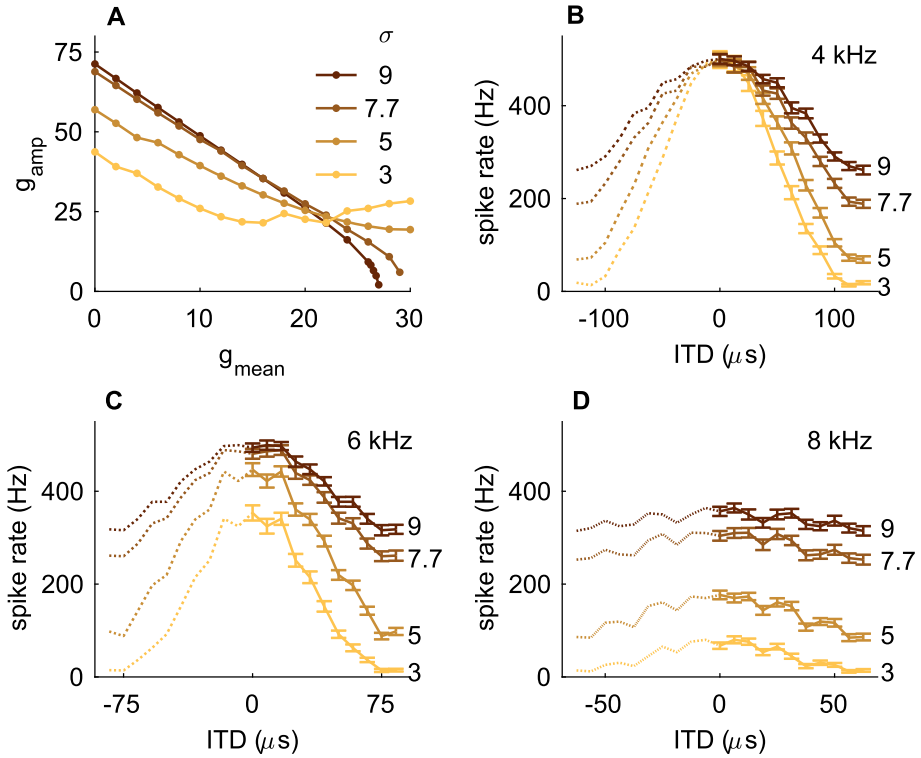

Fig. 8 Phasic dynamics enhance oscillation amplitude sensitivity and ITD tuning in the two-compartment NL model. **A** Thresholds for repetitive firing in response to 4 kHz sinusoidal conductance with varying mean (ordinate) and amplitude (abscissa). Compare to Fig. 4B and observe the slope of the threshold curves is less step, and can even turn positive, for phasic firing models (smaller σ). **B**–**D** ITD tuning curves (spike rate as function of input time difference) in response to 4 kHz (**B**), 6 kHz (**C**), and 8 kHz (**D**) synaptic inputs. Color code is same as Fig 3A. Tuning curves narrow for smaller σ demonstrating advantage of phasic firing for high-frequency ITD processing

rower tuning curves and greater peak-to-trough differences (ΔR). For the default parameter value of $\sigma = 7.7$ (tonic mode) the model fired vigorously to out-of-phase inputs (200 spikes/second, approximately). Out-of-phase firing is nearly extinguished for steepest sodium inactivation tested ($\sigma = 3$) while maintaining the criterion level of excitability to in-phase inputs (500 spikes/second). The benefits of phasic firing for ITD tuning persist in responses to higher-frequency inputs. ITD tuning curve depth is $\Delta R = 219$ spikes at 6 kHz and $\Delta R = 51$ spikes at 8 kHz for the original model setting $\sigma = 7.7$, tonic firing). These values increase to $\Delta R = 348$ spikes at 6 kHz and $\Delta R = 91$ spikes at 8 kHz for $\sigma = 5$ (phasic firing).

3 Discussion

Temporal precision is a hallmark of neural processing in the auditory pathway (Joris et al. 1994; Golding and Oertel 2012; Rose and Metherate 2005; Kayser et al. 2010; Moser et al. 2006). Sound localization on the basis of interaural time differences (ITDs) is one of the most temporally demanding aspects of auditory perception. Sound source location is encoded (in part) by submillisecond-scale time differences in sounds arriving at the two ears. Unraveling the physiological specializations of temporally precise binaural neurons has been the subject of sustained investigation. Features that specialize these neurons to act as temporally precise coincidence detectors include dendritic integration (Agmon-Snir et al. 1998; Golding and Oertel 2012; Winters et al. 2017; Mathews et al. 2010; Grau-Serrat et al. 2003), ionic currents active at subthreshold voltages (Svirskis et al. 2004; Huguet et al. 2017; Khurana et al. 2011), synaptic inputs (Jercog et al. 2010; Myoga et al. 2014; Grothe 2003; Fischl et al. 2012; Roberts et al. 2013) and spike generator regions in the axon at locations remote from the soma (Lehnert et al. 2014; Goldwyn et al. 2019; Kuba et al. 2006; Kuba 2012; Ashida et al. 2007).

3.1 Electrical separation of the soma and axon is essential high-frequency coincidence detection

We focused our attention on the dynamics of spike generation and the nature of soma–axon coupling since fine-tuning of soma–axon coupling may be particularly relevant for high-frequency ITD processing. In the nucleus laminaris (NL), where neurons can face the extreme challenge of extracting ITD information from kilohertz-scale inputs, previous

work has shown that spike initiation zones in the axon are more distant and smaller in size for neurons that have higher characteristic frequencies (Kuba et al. 2006). Computational modeling also showed that ITD sensitivity is improved if spike initiation occurs only in the axon, with the soma structured as large and passive (without sodium current) (Ashida et al. 2007). Similar structural advantages may help MSO neurons operate at the upper frequency limit of their ITD sensitivity (Scott et al. 2007; Lehnert et al. 2014; Goldwyn et al. 2019).

The advantage of remote spike initiation zone in NL neuron is typically explained by noting that this structural configuration impedes temporally summated inputs in the soma from invading the axon. Insulating the spike-generating region from sustained depolarization prevents inactivation of sodium channels that would suppress excitability (Kuba et al. 2006; Kuba 2012). In addition, impedance analysis indicates that the transfer of high-frequency voltage oscillations from soma to axon is greater if sodium current is absent from the soma region (Ashida et al. 2007). Synthesizing these arguments, one could conclude that soma–axon connections in NL neurons should act as high-pass filters. There should be minimal attenuation (or even amplification) in the transfer of high-frequency voltage oscillations to the axon, but mean soma voltage or slow variations in soma voltage should not pass to the axon.

Using a signal detection analogy, we considered these same requirements but from the point of view of axonal spiking as a means to monitor ITD information present in the oscillating inputs to NL neurons. Informed by current understanding of NL responses to high-frequency pure tone inputs (the sound analogue potential, SAP, as measured in (Funabiki et al. 2011) and studied further in (Ashida et al. 2013a, b)), our view is that spike generation in NL neurons should be insensitive to slowly varying changes in inputs (the kinds of changes that would be associated with temporal summation of non-coincident inputs). Instead, NL neurons should fire in response to the high-frequency oscillations that are evoked by coincident synaptic events. Said differently, we concur that NL neurons should have high-pass-like behavior to be effective ITD processors, but we locate mechanisms for high-pass-like behavior in several nonlinear aspects of NL spiking dynamics.

We showed that high-frequency ITD sensitivity is severely degraded by strong electrical coupling between the soma and spike-generating regions (Fig. 3). Strong soma–axon coupling allows for sodium in the axon to act as a source of nonlinear amplification of subthreshold inputs in the soma (Fig. 5A, B). This causes neural excitability to depend on mean input level (Fig. 4B). Structural configurations with weaker soma–axon coupling linearly integrate subthreshold inputs and thus respond more selectively to oscillation amplitude. This is consistent with a previous finding that a passive soma enhances coincidence detection in an NL model because sodium in the soma nonlinearly amplifies subthreshold inputs (Ashida et al. 2007). In addition, strong coupling slows the speed of spike initiation (which we measured as the slope spike upstroke, Fig. 5C). Similar observations about the relationship between spike upstroke and soma–axon coupling have been made previously (Brette 2013). Fast spike initiation aids in responding to high-frequency input (Fourcaud-Trocmé et al. 2003; Scott et al. 2007; Huang et al. 2012), so this is a second reason why electrical separation of the soma from the axon enhances high-frequency ITD sensitivity.

If insulation from temporally summating inputs (to prevent sodium inactivation in the axon) was a primary benefit of weak soma-to-axon coupling, one might expect that ITD sensitivity should decrease in our model with increases in the forward coupling constant. Some minor trends to this effect are evident in Fig. 3B for configurations with strong backward coupling. For weaker backward coupling, though, ITD sensitivity does not depend on forward coupling strength. Recall that we selected sodium conductance separately for each coupling configuration. For instance, maximum sodium conductance is $g_{\mathrm{Na}} = 4304$ nS for the $(\kappa_{1\to2}, \kappa_{2\to1}) = (0.3, 0.2)$ configuration and is $g_{\mathrm{Na}} = 428$ nS for the $(\kappa_{1\to2}, \kappa_{2\to1}) = (0.9, 0.2)$ configuration. Reducing sodium conductance with increases in forward coupling strength may explain why we did not find that strong forward coupling, on its own, degrades ITD sensitivity by inactivating sodium currents.

3.2 Phasicness, a generic mechanism for neural coincidence detection, also improves high-frequency ITD processing

NL neurons exhibit phasic firing in vitro (Reyes et al 1996), but the Hodgkin–Huxley-type models developed for NL neurons do not (Ashida et al. 2007; Funabiki et al. 2011). We determined that our model became more sensitive to oscillation amplitude and less sensitive to input mean when it was converted to the phasic firing mode (Fig. 8A). In addition, phasic firing resulted in improved ITD tuning (Fig. 8B).

We steepened the sodium inactivation steady-state curve $h_\infty(V)$ as a straightforward way to convert the model to phasic firing (see also Meng et al. (2012)). A previous study of coincidence detection and temporal precision in MSO neurons left-shifted the $h_\infty(V)$ curve as a means to toggle between phasic and tonic firing (Huguet et al. 2017). Either manipulation of $h_\infty(V)$ creates phasic firing dynamics because they strengthen the negative feedback effect produced by sodium inactivation at subthreshold voltage levels (Huguet et al. 2017).

If a model is in a tonic firing mode, then it can be tipped into a repetitive firing pattern by temporal summation of

high-frequency inputs. This can be problematic for modeling NL neural activity because voltage responses in the soma that trigger spikes are small-amplitude events (SAP oscillations on the order of a few millivolts) (Funabiki et al. 2011). Sodium current in these models must be carefully calibrated, therefore, so that small-amplitude oscillations can evoke spikes but temporal summation of inputs do not (Grau-Serrat et al. 2003). In past modeling studies, mean input levels have been selected to position the dynamics near the boundary of critical points for repetitive firing (Ashida et al. 2007) or have used *ad hoc* synaptic normalization rules to suppress the mean input (temporally summated synaptic inputs). Some amount of fine-tuning is necessary for these neurons because of the nature of their synaptic inputs and the temporally demanding computation they perform. Indeed, developmental and homeostatic processes do regulate axon physiology in NL neurons and their inputs (Kuba et al. 2006; Kuba 2012). Nonetheless, phasic firing is clearly a more robust mode of excitability. Phasic excitability creates selectivity for input variance while preventing excitation by background level or slowly varying inputs (Meng et al. 2012; Lundstrom et al. 2008, 2009).

3.3 Toward a unified view of binaural coincidence detector neurons

We have found ITD sensitivity to be enhanced if soma and axon regions are electrically separated in an NL neuron model, and that phasic dynamics further enhance the function of these as temporally precise coincidence detectors. Similar specializations may enhance ITD processing by MSO neurons in mammals (Scott et al. 2007; Lehnert et al. 2014; Goldwyn et al. 2019), suggesting common dynamic principles at work in these different neural systems. While these neurons may operate at different frequency regions and in the context of cross-species differences in their auditory pathways, they appear to share many physiological features. We have remarked that both MSO and NL neurons exhibit phasic firing. In addition, they are both characterized by several related physiological features (low input resistance, fast membrane time constant, prominent voltage-gated currents active at subthreshold voltage levels). That being said, there are also notable differences in these two circuits, including in the numbers and types of synaptic inputs (Ashida and Carr 2011, for review). Continued explorations of the similarities and differences between these centers for binaural coincidence detection can clarify the function of MSO neurons with high characteristic frequency (Gai et al. 2009; Remme et al. 2014) and may also provide insights into how ITD information can be delivered with the high-frequency stimuli used in cochlear implant technology (Laback et al. 2015; Buechel et al. 2018).

A prominent low-threshold potassium current that is active at subthreshold voltages is common to both MSO and NL neurons. In MSO neurons, this voltage-gated current acts as a dynamic negative feedback mechanism that enhances temporally precise coincidence detection (Svirskis et al. 2003, 2004; Jercog et al. 2010; Mathews et al. 2010). In the previous work, we have observed that KLT current improves ITD sensitivity in two-compartment neuron models, especially when the current is colocated with spike-generating sodium current in the axon compartment (Goldwyn et al. 2019). The role of KLT in NL neurons is less understood. The high-frequency signals we considered in this study, as representative of the frequencies encountered by the ITD processing circuit in the barn owl, oscillate on timescales faster than the timescales of KLT activation and inactivation dynamics. In their NL simulations, Ashida and colleagues found that low-threshold potassium current rendered their model "more tolerant to changes in DC amplitude" (Ashida et al. 2007). In light of our findings, we interpret their observation to mean that the negative feedback effect of KLT is advantageous for high-frequency ITD sensitivity because it can prevent supralinear amplification of subthreshold inputs, which we found to be detrimental to high-frequency ITD sensitivity.

Another feature of binaural neurons and circuits that we did not include in our model, but that can be understood in relation to our findings is inhibition. Inhibitory feedback from the superior olivary nucleus improved ITD sensitivity in a model of NL circuit in chicken (Dasika et al. 2005). Inhibitory feedback that stabilizes mean input level (counteracting sustained depolarization due to temporal summation) would help the NL circuit transmit ITD information via high-frequency oscillating inputs. The function of inhibition in MSO neurons continues to be studied (Grothe 2003; Couchman et al. 2010; Goldwyn et al. 2017; Winters and Golding 2018) with evidence that precisely time inhibitory inputs shift the peaks of ITD tuning curves (Brand et al. 2002; Pecka et al. 2008; Jercog et al. 2010; Myoga et al. 2014) (but see also Roberts et al. (2013); Franken et al. (2015)).

In sum, the remarkable temporal precision of binaural coincidence detector neurons requires numerous cellular and circuit-based specializations. Tracing these intriguing cross-species similarities between MSO and NL neurons provides useful perspectives on both systems. We have emphasized that the nature of high-frequency synaptic inputs requires NL neurons to respond selectively to oscillation amplitude, not mean input level. Low-frequency ITD encoding in the MSO, in contrast, requires slope-sensitive neurons to respond selectively to a few well-timed inputs (Meng et al. 2012; Remme et al. 2014; Jercog et al. 2010; Svirskis et al. 2004). Taken together, our findings add to the evidence that there are shared structural and dynamical principles underlying the encoding of sound source location by neural coincidence across different species and widely different frequency ranges.

4 Methods

4.1 Two-compartment NL neuron model

We studied spiking dynamics of a barn owl NL neuron using a two-compartment model that was previously and applied to *in vivo* physiology (Ashida et al. 2007; Funabiki et al. 2011). The model consists of a compartment with passive dynamics (compartment 1 with voltage variable V_1, representing the soma region) and a compartment with excitable dynamics (compartment 2 with voltage variable V_2, representing a spike-initiating node in the axon). Separating the NL soma and axon regions is common practice in the models that we build upon and is justified by anatomical observation that the soma is separated from spike initiation zones in NL axons by a myelinated axon initial segment Carr and Boudreau (1993). Voltages in the two compartments are governed by coupled differential equations

$$\begin{aligned} c_1\frac{\mathrm{d}V_1}{\mathrm{d}t} &= -g_{lk,1}(V_1 - E_{lk,1}) - g_{ax}(V_1 - V_2) - I_{\mathrm{in}}(t) \\ c_2\frac{\mathrm{d}V_2}{\mathrm{d}t} &= -g_{lk,2}(V_2 - E_{lk,2}) - g_{ax}(V_2 - V_1) \\ &\quad - I_{\mathrm{Na}}(V_2) - I_{\mathrm{KHT}}(V_2) \end{aligned} \tag{1}$$

where capacitance (c), leak conductance (g_{lk}) and leak reversal potential (E_{lk}) can take different values in each compartment. The axial conductance g_{ax} is the Ohmic coupling between the two compartments. The input current to the soma I_{in} typically represents either sinusoidal input current or conductance-based synaptic inputs. Voltage-gated ionic currents in the axon are spike-generating sodium current (I_{Na}) and high-threshold potassium current I_{KHT}. More details regarding these currents are given below.

We adapt the model by varying the leak and axial conductances in a principled manner (detailed below). Our method allows us to explore a large parameter space while constraining response properties in the input compartment (V_1) to match the reported physiology in the NL soma (input conductance, membrane time constant, resting potential). Dynamics in the spiking compartment (V_2) are affected by our parameter variations. NL axon physiology (spike shape, for instance) has not been reported, to our knowledge. We view, therefore, this parameter exploration as a natural use of a computational model with parameters that could further refined by future physiological data.

4.2 Passive parameters determined by soma–axon coupling

Following the method described in (Goldwyn et al. 2019), we set passive parameter values so that V_1 dynamics reproduced basic, physiologically measurable properties of NL neurons (resting potential, input resistance and membrane time constant). We then created a two-parameter space described by the strength of forward and backward couplings between the two compartments. With this approach, we could study ITD sensitivity while systematically varying soma–axon coupling configurations (Goldwyn et al. 2019; Franken et al. 2021).

We set passive parameter values using values of three physiological constants similar to what has been reported in a previous studies of NL neurons (Funabiki et al. 2011). These are input resistance in the soma ($R_1 = 5\,\mathrm{M}\Omega$), resting potential in the soma ($E_{\mathrm{rest}} = -62$ mV, also used for V_2 resting voltage) and soma membrane time constant describing the timescale of exponential decay of V_1 ($\tau_{\mathrm{exp}} = 0.1$ ms). We assumed the surface area of the first compartment is orders of magnitude larger than the surface area of the second compartment (2400 $\mu\mathrm{m}^2$ compared to 20 $\mu\mathrm{m}^2$), consistent with previous NL modeling studies following (Ashida et al. 2007; Funabiki et al. 2011).

We followed the approach in Goldwyn et al. (2019) to determine passive parameters in the two-compartment model. This enables systematic variation of coupling configuration will maintaining nearly identical passive V_1 dynamics. Defining U_1 and U_2 to be the deviations of voltages from rest and removing the voltage-gated currents I_{Na} and I_{KHT}, the passive dynamics relative to rest are:

$$\begin{aligned} \tau_1\frac{\mathrm{d}U_1}{\mathrm{d}t} &= -U_1 + \kappa_{2\to1}U_2 - J_{\mathrm{in}}(t) \\ \tau_2\frac{\mathrm{d}U_2}{\mathrm{d}t} &= -U_2 + \kappa_{1\to2}U_1 \end{aligned} \tag{2}$$

where the time constant parameters $\tau_i = c_i/(g_i + g_{ax})$ for $i = 1, 2$ and $J_{\mathrm{in}} = I_{in}/(g_1 + g_{ax})$ is a rescaled input term. The soma-to-axon (forward) coupling parameter $\kappa_{1\to2}$ and axon-to-soma (backward) coupling parameter $\kappa_{2\to1}$ describe the impact of voltage deviations in one compartment on the other. Alternatively, these parameters can be thought of as steady-state attenuation factors between the two compartments. They are

$$\kappa_{i\to j} = g_c/(g_j + g_c) \qquad \text{for } i, j = 1, 2 \text{ with } i \neq j. \tag{3}$$

Due to the large discrepancy in membrane surface areas, there is a timescale separation between the passive dynamics in the two compartments (V_2 is fast relative to V_1). In particular, the ratio of time constants is $\tau_2/\tau_1 = \alpha\kappa_{1\to2}/\kappa_{2\to1}$. For $\alpha = 20/2400$ (as specified above) and the range of coupling constants used in our study, we have that τ_2 takes values approximately 10 to 100 times smaller than τ_1. Due to this separation of timescales, we could use fast–slow analysis to uniquely define combinations of passive parameters that vary soma–axon coupling while maintaining nearly identical passive dynamics in the soma compartment (see Goldwyn et al. 2019 for details):

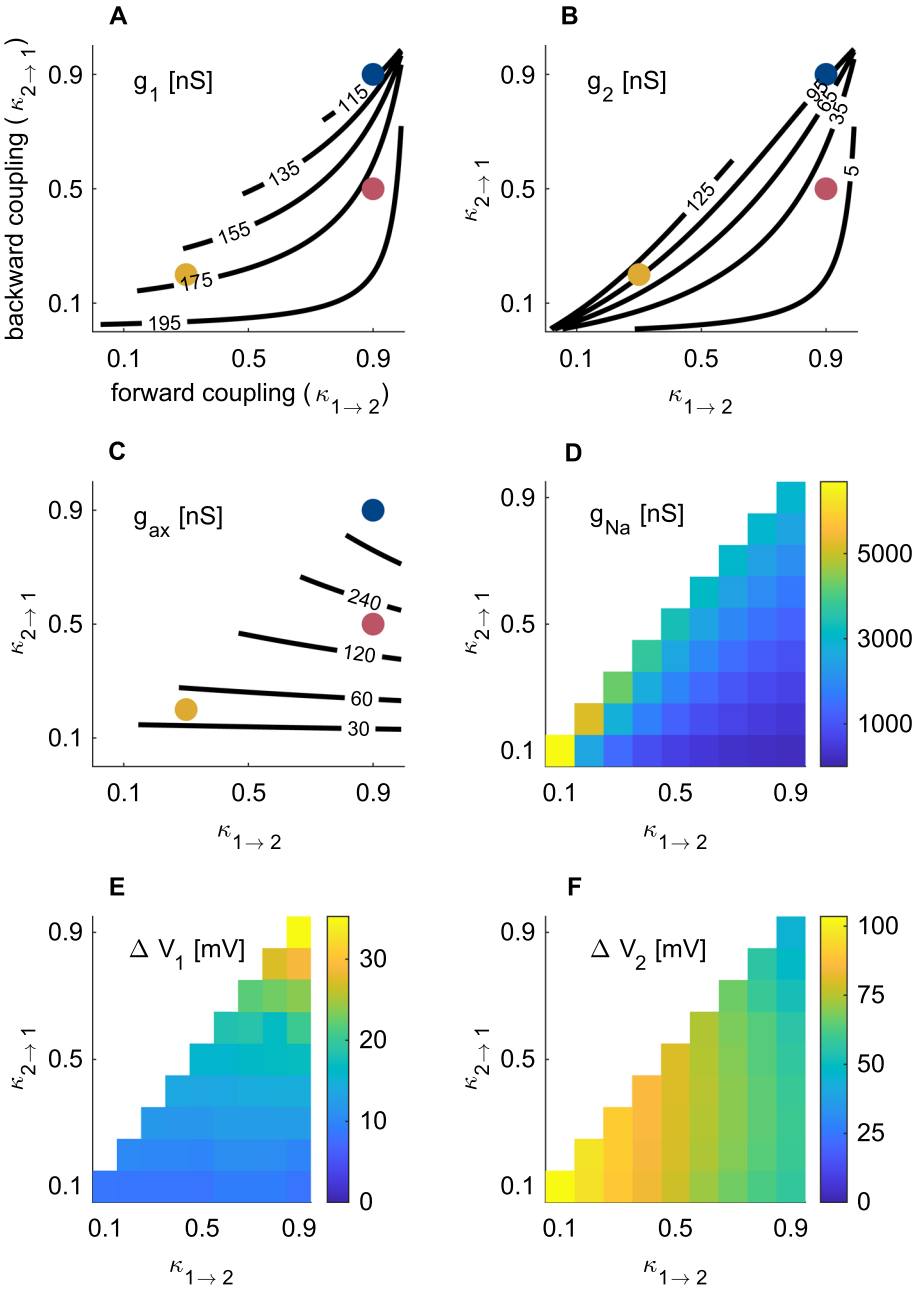

Fig. 9 Parameter space for two-compartment NL model. **A** Total conductance in the soma compartment (g_1). **B** Total conductance in the axon compartment (g_2). **C** Axial conductance between the two compartments (g_{ax}). Parameters in **A**–**C** depend uniquely on soma–axon coupling constants and commonly reported physiological properties (input resistance and membrane time constant in the soma) and are determined for a passive model. Colored dots mark the specific coupling configurations used in many figures (refer to Fig. 2). We used, as a reference value $\kappa_{1\to2} = 0.9$ and $\kappa_{2\to1} = 0.5$ since this configuration is similar to the parameter set used in (Funabiki et al. 2011). **D** Sodium conductance in the axon compartment (g_{Na}). This parameter is determined so that, at each coupling configuration, the model fired at 500 spikes/sec at ITD = 0 μs. **E** Maximum voltage range in soma compartment in response to 4 kHz in-phase synaptic input. **F** Maximum voltage range in axon compartment from same responses as in **E**

$$
\begin{aligned}
g_{ax} &= \frac{\kappa_{2\to1}}{R_1(1-\kappa_{1\to2}\kappa_{2\to1})} \\
g_1 &= g_{ax}\left(\frac{1}{\kappa_{2\to1}}-1\right) \\
g_2 &= g_{ax}\left(\frac{1}{\kappa_{1\to2}}-1\right) \\
c_1 &= \tau_{\text{exp}}(1-\kappa_{1\to2}\kappa_{2\to1})(g_1+g_{ax}) \\
c_2 &= \alpha c_1
\end{aligned}
\tag{4}
$$

Values of these parameters throughout the coupling parameter space are shown in Fig. 9A–C.

4.2.1 Voltage-gated spike-generating currents

The voltage-gated currents in the axon region are the spike-generating sodium current I_{Na} and the high-threshold potassium current I_{KHT}. We modeled the dynamics of these currents as in (Funabiki et al. 2011):

$$
\begin{aligned}
I_{\text{Na}}(V_2) &= g_{\text{Na}} m h (V_2 - E_{\text{Na}}) \\
&\quad - m_\infty(V_{\text{rest}}) h_\infty(V_{\text{rest}})(V_{\text{rest}} - E_{\text{Na}}) \\
I_{\text{KHT}}(V_2) &= g_{\text{KHT}} n (V_2 - E_{\text{Na}}) \\
&\quad - n_\infty(V_{\text{rest}})(V_{\text{rest}} - E_{\text{Na}}).
\end{aligned}
\tag{5}
$$

We include the second term so that these currents are zero at rest. This facilitates our exploration of coupling parameter space. This can be implemented equivalently as a shift in the leak reversal potential. Reversal potentials are $E_{\text{Na}} = 35$ mV and $E_K = -75$ mV.

We set maximal sodium conductance g_{Na} separately for each coupling configuration to achieve a consistent firing rate response of 500 spikes per second to in-phase synaptic inputs. We selected this criterion to be similar to the peak firing rate reported in previous modeling work (Funabiki et al. 2011; Ashida et al. 2013b). We found g_{Na} values to range from 200 to 7000 nS, roughly (Fig. 9D). Coupling configuration and sodium conductance determine the shape of action potentials in the axon and the extent to which spikes back-propagate into the soma. Spikes in the soma of NL neurons are small (around 10 mV in Funabiki et al. (2011)). As a rough measure of spike size, we measured the maximum voltage ranges in the two compartments. This is ΔV in Fig. 9E, F. It is calculated as the maximum voltage minus the minimum voltage, where the extreme values of voltage were measured over the duration of a response to 4 kHz synaptic inputs with ITD = 0 μs. The ranges of ΔV_1 show small spikes in the soma and show spike sizes decrease as the backward coupling strength ($\kappa_{2\to1}$) decreases. The range of ΔV_2 show large, "fully formed" spikes that are larger for configurations with weaker forward coupling (smaller $\kappa_{1\to2}$). If the spike generator is not electrically isolated from the soma, then the soma acts as a strong sink that decreases spike amplitude. Recalling that Funabiki and colleagues parameterized this model, for their study of in vivo NL activity, so that $\kappa_{1\to2} \approx 0.9$ and $\kappa_{2\to1} \approx 0.5$, we observe that a large portion of the coupling parameter space produces spikes in the soma similar to their model setting. In fact, since spike size in the soma is predominantly determined by the backward coupling constant, we can view the backward coupling constant $\kappa_{2\to1}$ as (roughly) a free parameter that requires future physiological data to specify more precisely (e.g., axonal recordings).

Table 1 Voltage-gated ion channel subunit kinetics

Na activation (m)
$\alpha_m(V) = 3.6e^{(V+34)/7.5}$
$\beta_m(V) = 3.6e^{-(V+34)/10}$
Na inactivation (h)
$\alpha_h(V) = 0.6e^{-(V+34)/18}$
$\beta_h(V) = 0.6e^{(V+34)/13.5}$
KHT activation (n)
$\alpha_n(V) = 0.110e^{(V+19.)/9.1}$
$\beta_n(V) = 0.103e^{-(V+19.)/20}$

We set the maximal high-threshold potassium conductance to $g_{\text{KHT}} = 0.3 g_{\text{Na}}$ as in (Funabiki et al. 2011). The passive leak conductance in the axon ($g_{lk,2}$ in Eq 1) was reduced by amounts equal to g_{Na} and g_{KHT} to maintain the total axon conductance at rest determined by the initial parameter-fitting calculation (g_2 in Eq. 4). We did not include any voltage-gated currents in the soma (as in Ashida et al. 2007), so leak conductance in the soma compartment is identical to g_1.

The kinetics of the gating variables are governed by equations of the form

$$
\frac{\mathrm{d}u}{\mathrm{d}t} = \phi\left(\frac{u_\infty(V_2) - u}{\tau_u(V_2)}\right) \qquad (\text{for } u = m, h, n). \tag{6}
$$

The constant $\phi = 4.75$ adjusts for temperature at 40° C with Q10 factor 2.5. The functions u_∞ and τ_u are identical to the model in Funabiki et al. (2011) using the conventional definitions that $u_\infty(V) = \alpha_u(V)/(\alpha_u(V) + \beta_u(V))$ and $\tau_u(V) = 1/(\alpha_u(V) + \beta_u(V))$ where α_u and β_u represent opening and closing rates, respectively, for voltage-gated ion channel subunits (Table 1).

4.2.2 Modification of sodium inactivation for phasic model

We created a phasic version of the model by altering the steady-state function for sodium inactivation (h_∞). The default definition of h_∞ using the values of the α_h and β_h

given in Table 1 is

$$h_\infty(V) = \frac{1}{1 + e^{(V+57)/\sigma}} \tag{7}$$

where $\sigma = 7.7$ reproduces the model in Funabiki et al. (2011). We found that reducing σ (resulting in steeper h_∞ curve) was a practical way to toggle the model between a tonic firing mode (at the default σ value) and a phasic firing mode (for smaller σ values). We recalculated maximal sodium conductance separately for each σ value to maintain the consistent peak firing rate of 500 spikes/sec. It was necessary to increase g_{Na} for smaller values of σ. For the coupling configuration $\kappa_{1\to2} = 0.9$ and $\kappa_{2\to1} = 0.5$, for example, g_{Na} increased from 1240 nS for $\sigma = 9$ to 1838 nS for $\sigma = 3$.

4.2.3 Synaptic current and the SAP

We modeled input currents I_{in} as either a sinusoidally varying conductance (an idealized description of the high-frequency oscillatory input to NL neurons) (Ashida et al. 2007; Funabiki et al. 2011; Ashida et al. 2013a) or as the summed input of simulated excitatory synaptic events. In the first case (idealized sinusoidal input), the parameter g_0 is the baseline (mean) level of the input conductance and g_1 is the amplitude of input oscillations. The reversal potential is $E_{\mathrm{syn}} = 0$ mV for both input types. We used f between 4000 Hz and 8000 Hz in all simulations in this study. This value is in the range of high-frequency tones that barn owls can localize and has been used in previous modeling studies (Funabiki et al. 2011; Ashida et al. 2007, 2013b). Our rationale for this idealized input is that tone-evoked voltage responses in the soma of NL neurons are characterized by oscillations at the tone frequency (the so-called sound analogue potential, SAP) and that SAP amplitude (not baseline level) varies with ITD (Funabiki et al. 2011). The parameter g_1 controls the amplitude of this idealized input with large g_1 interpreted to represent preferred ITDs with coincident inputs that drive maximal firing.

For simulations in which we preferred a more biophysically realistic description of the ITD computation performed by NL neurons, we let $I_{\mathrm{in}}(t) = g(t)(E_{\mathrm{syn}} - V_1)$ where $g(t)$ represents synaptic conductance generated by simulated trains of synaptic events filtered by short-duration excitatory postsynaptic potentials (EPSGs):

$$g(t) = \sum_{n=1}^{N} \sum_{t_{i,n}} g_s s(t - t_{i,n}). \tag{8}$$

We used the synaptic model of Ashida and colleagues (Ashida et al. 2013a, b) and parameters drawn from their work. Synaptic reversal potential is $E_{\mathrm{syn}} = 0$ mV (as above) and the time course of synaptic conductance $g(t)$ is a random process constructed as the sum of unitary EPSG events produced by N independent input neurons whose event times $t_{i,n}$ are sampled from an inhomogeneous Poisson process. The Poisson intensity $\lambda(t)$ is the periodic function $\lambda(t) = 2\pi\lambda_0 p_k(2\pi f t)$, where f is the input frequency, λ_0 is the baseline rate (500 Hz) and p_κ is the von Mises distribution function with concentration parameter κ (see Ashida et al. 2013a, b for details). The unitary EPSG events are alpha functions

$$s(t - t_i) = \begin{cases} 0 & \text{for } t < t_{i,n} \\ (g_s t/\tau_{\mathrm{syn}}) e^{1 - t/\tau_{syn}} & \text{for } t \geq t_{i,n} \end{cases} \tag{9}$$

with maximal conductance $g_0 = 1.3$ nS and time constant $\tau_{\mathrm{syn}} = 40.9$ μs. This exceptionally brief time constant is required for the model to replicate properties of the SAP observed in vivo (Funabiki et al. 2011; Ashida et al. 2013a, b). We used $N = 300$ for the total number of inputs (NM neurons), evenly divided into two input streams to simulate binaural (two-eared) inputs. Synaptic inputs carry ITDs when there is a time lag between the time courses of $\lambda(t)$ used in each of the two NM population representing the two "ears."

4.3 Measure of coincidence detection sensitivity and ITD coding

We simulated the sound localization computation performed by NL neurons by measuring mean firing rate of the two-compartment model in response to repeated samples from the synaptic input model. Spikes (defined as an upward crossing of V_2 past −30 mV) were counted over a duration of 20 ms and mean spike rates were averages from 100 repetitions.

As a summary measure of ITD sensitivity we calculated the difference between in-phase and out-of-phase mean firing rates (visualized as the peak-to-trough difference in ITD tuning curve height). We denoted this statistic as ΔR and note that it has been used commonly used in previous studies of ITD processing including for NL neurons (Ashida et al. 2007; Funabiki et al. 2011; Grau-Serrat et al. 2003).

We calculated thresholds for repetitive spiking in response to sinusoidal input conductance. Repetitive firing to these inputs was defined as more than one spike in both halves of the 20-ms-long stimulus. Threshold for repetitive firing was defined as the smallest possible input strength at which repetitive firing could be observed over a range of initial values. A modified bisection search method was used so that, with g_0 fixed, g_1 thresholds were calculated to within ±0.5 nS. As part of the bisection search, we found it necessary to systemically test a range of initial values in order to identify the minimum threshold in cases when the model exhibited hysteresis dynamics.

4.4 Numerical methods

Original simulation code was developed in C, Python and MATLAB and is available at https://github.com/jhgoldwyn/TwoCompartmentNL. Computations to determine g_{Na} conductance values and measure ITD tuning curves were performed on a multi-CPU cluster maintained by Swarthmore College. All other computations were performed on personal laptops. Two-compartment model simulations were carried out using the forward Euler method with a 0.1 μs time step. Synaptic conductance time courses ($g(t)$ in Eq 8) were also computed at this temporal resolution. For some coupling configurations (those with large g_{Na} values), we found it necessary to use smaller time step sizes in the Euler calculations, in which case we linearly interpolated synaptic conductance time courses to the smaller time steps.

4.5 Synaptic classification by Fisher's linear discriminant

As conceptual support for how to understand the coincidence detection computation performed by NL neurons, we considered how in-phase and out-of-phase inputs could be linearly separated (Fig. 4A). Specifically, for every period of the 4 kHz stimulus, we measured the mean and amplitude (half the maximum-to-minimum range of $g(t)$) of synaptic input currents for one-second-long samples of the biophysically based synaptic input model (see above). We then used Fisher's linear discriminant to find the direction $\mathbf{w}$ along which to project these data in order to maximally separate them in-phase from out-of-phase synaptic inputs. Let $\mathbf{x}_n$ be the vector containing the mean and amplitude of $g(t)$ on each period of an in-phase input, $\mathbf{y}_n$ the corresponding vector for out-of-phase inputs, and denote the means of these values (over all periods of the input) as $\langle \mathbf{x} \rangle$ and $\langle \mathbf{y} \rangle$, respectively. Then Fisher's linear discriminant for optimally separating the in-phase and out-of-phase inputs on a cycle-by-cycle basis is to project these data onto any vector $\mathbf{w}$ in the direction of $\Sigma_W^{-1}(\mathbf{m}_1 - \mathbf{m}_2)$ (Bishop 2006), where Σ_W is the within-class covariance matrix

$$\Sigma_W = \sum_n (\mathbf{x}_n - \langle \mathbf{x} \rangle)^T (\mathbf{x}_n - \langle \mathbf{x} \rangle) + \sum_n (\mathbf{y}_n - \langle \mathbf{y} \rangle)^T (\mathbf{y}_n - \langle \mathbf{y} \rangle).$$

4.6 Nonlinear integrate-and-fire model

Two features of nonlinear dynamics in the axon that we found could impact coincidence detection sensitivity are the quickness of spike initiation and the extent to which sodium current in the axon amplifies subthreshold voltages in the soma (causing the input region to deviate from linear, passive dynamics). We developed a nonlinear integrate-and-fire mode to investigate these two features. The dynamical variable of the model is $x(t)$, a voltage-like variable, that is governed by separate rules for subthreshold and suprathreshold (spike initiation) behavior. We formulated these subthreshold and suprathreshold rules simply in order to have direct parameter control over the dynamics in these separate regimes:

$$\begin{cases} \tau \frac{\mathrm{d}x(t)}{\mathrm{d}t} = f(x(t)) + a + b\sin(2\pi f t) \\ \qquad\qquad \text{if } x(t) < x_{\mathrm{thresh}} \\ \tau \frac{\mathrm{d}x(t)}{\mathrm{d}t} = q(x(t) - x_{\mathrm{thresh}}) + a + b\sin(2\pi f t) \\ \qquad\qquad \text{if } x_{\mathrm{thresh}} \le x(t) < x_{\mathrm{max}} \\ x(t) = x_{\mathrm{reset}} \text{ if } x(t) \ge x_{\mathrm{max}} \end{cases} \tag{10}$$

where the function $f(x)$ has the form

$$f(x) = \begin{cases} -x & \text{if } x \le 0 \\ (p-1)x - p\left(\frac{x}{1+x}\right) & \text{if } 0 \le x < x_{\mathrm{thresh}} \end{cases}. \tag{11}$$

We view the piecewise nonlinearity in $f(x)$ as a caricature of the amplifying effect that sodium current in the axon can have if there is sufficient backpropagation from axon to soma (strong backward coupling), as shown in Fig. 5A, B. In particular, the parameter p interpolates between linear subthreshold dynamics ($p = 0$) and supralinear subthreshold dynamics ($p = 1$).

Spike generation in the model in two phases. First, if $x(t)$ exceeds the spike initiation threshold x_{thresh}, then $x(t)$ increases with the exponential growth rate q. We set $x_{\mathrm{thresh}} = 1$ for the linear model ($p = 0$) and $x_{\mathrm{thresh}} = 1.25$ for the nonlinear model ($p = 1$) to maintain the same AC threshold at when DC=0 (same y-axis intercept in Fig. 6. Second, spike generation occurs at the instant at which $x(t)$ exceeds $x_{\mathrm{max}} = 50$, at which point the value of $x(t)$ resets to $x_{\mathrm{reset}} = -5$. We use the exponential growth parameter q to characterize the slope of spike upstroke, which we observed could change with coupling configuration (Fig. 5C). The integrate-and-fire model was simulated in MATLAB with code available at https://github.com/jhgoldwyn/TwoCompartmentNL.

Acknowledgements This work used the Strelka Computing Cluster at Swarthmore College, which is supported by the Swarthmore College Office of the Provost.

Author Contributions JHG was involved in conceptualization, funding acquisition and supervision. BD and JHG were responsible for methodology, formal analysis and investigation, writing—original draft preparation and writing—review and editing. JHG conceived of and supervised the project. Both authors conducted simulations and analysis, prepared figures, and wrote and revised the manuscript.

Funding This research was supported NSF-DMS 1951436 awarded to JHG. The funders had no role in study design, data collection and analysis, decision to publish or preparation of the manuscript.

Data availability Not applicable.

Code availability Original simulation code was developed in C, Python and MATLAB and is available at https://github.com/jhgoldwyn/TwoCompartmentNL

Declarations

Conflict of interest The authors have no competing interests to declare that are relevant to the content of this article.

Ethics approval Not applicable.

Consent to participate Not applicable.

Consent for publication Not applicable.

References

Agmon-Snir H, Carr CE, Rinzel J (1998) The role of dendrites in auditory coincidence detection. Nature 393(6682):268–272. https://doi.org/10.1038/30505

Ashida G, Carr CE (2011) Sound localization: Jeffress and beyond. Curr Opin Neurobiol 21(5):745–751. https://doi.org/10.1016/j.conb.2011.05.008

Ashida G, Abe K, Funabiki K et al (2007) Passive soma facilitates submillisecond coincidence detection in the owl's auditory system. J Neurophysiol 97(3):2267–2282. https://doi.org/10.1152/jn.00399.2006

Ashida G, Funabiki K, Carr C (2013a) Theoretical foundations of the sound analog membrane potential that underlies coincidence detection in the barn owl. Front Comput Neurosci 7:151. https://doi.org/10.3389/fncom.2013.00151

Ashida G, Funabiki K, Carr CE (2013b) Biophysical basis of the sound analog membrane potential that underlies coincidence detection in the barn owl. Front Comput Neurosci. https://doi.org/10.3389/fncom.2013.00102

Batra R, Kuwada S, Fitzpatrick DC (1997) Sensitivity to interaural temporal disparities of low- and high-frequency neurons in the superior olivary complex. II. coincidence detection. J Neurophysiol 78(3):1237–1247. https://doi.org/10.1152/jn.1997.78.3.1237

Bishop CM (2006) Pattern recognition and machine learning. Springer, New York. https://doi.org/10.1007/978-0-387-45528-0

Brand A, Behrend O, Marquardt T et al (2002) Precise inhibition is essential for microsecond interaural time difference coding. Nature 417(6888):543–547. https://doi.org/10.1038/417543a

Brette R (2013) Sharpness of spike initiation in neurons explained by compartmentalization. PLoS Comput Biol 9(12):e1003338. https://doi.org/10.1371/journal.pcbi.1003338

Buechel BD, Hancock KE, Chung Y et al (2018) Improved neural coding of ITD with bilateral cochlear implants by introducing short inter-pulse intervals. J Assoc Res Otolaryngol 19(6):681–702. https://doi.org/10.1007/s10162-018-00693-0

Carr C, Boudreau R (1993) An axon with a myelinated initial segment in the bird auditory system. Brain Res 628(1–2):330–334. https://doi.org/10.1016/0006-8993(93)90975-s

Carr C, Konishi M (1990) A circuit for detection of interaural time differences in the brain stem of the barn owl. J Neurosci 10(10):3227–3246. https://doi.org/10.1523/jneurosci.10-10-03227.1990

Carr CE, Konishi M (1988) Axonal delay lines for time measurement in the owl's brainstem. Proc Natl Acad Sci 85(21):8311–8315. https://doi.org/10.1073/pnas.85.21.8311

Couchman K, Grothe B, Felmy F (2010) Medial superior olivary neurons receive surprisingly few excitatory and inhibitory inputs with balanced strength and short-term dynamics. J Neurosci 30(50):17111–17121. https://doi.org/10.1523/jneurosci.1760-10.2010

Dasika VK, White JA, Carney LH et al (2005) Effects of inhibitory feedback in a network model of avian brain stem. J Neurophysiol 94(1):400–414. https://doi.org/10.1152/jn.01065.2004

Fischl MJ, Combs TD, Klug A et al (2012) Modulation of synaptic input by $GABA_B$ receptors improves coincidence detection for computation of sound location. J Physiol 590(13):3047–3066. https://doi.org/10.1113/jphysiol.2011.226233

Fourcaud-Trocmé N, Hansel D, van Vreeswijk C et al (2003) How spike generation mechanisms determine the neuronal response to fluctuating inputs. J Neurosci 23(37):11628–11640. https://doi.org/10.1523/jneurosci.23-37-11628.2003

Franken TP, Roberts MT, Wei L et al (2015) In vivo coincidence detection in mammalian sound localization generates phase delays. Nat Neurosci 18(3):444–452. https://doi.org/10.1038/nn.3948

Franken TP, Bondy BJ, Haimes DB et al (2021) Glycinergic axonal inhibition subserves acute spatial sensitivity to sudden increases in sound intensity. eLife. https://doi.org/10.7554/elife.62183

Funabiki K, Ashida G, Konishi M (2011) Computation of interaural time difference in the owl's coincidence detector neurons. J Neurosci 31(43):15245–15256. https://doi.org/10.1523/jneurosci.2127-11.2011

Gai Y, Doiron B, Kotak V et al (2009) Noise-gated encoding of slow inputs by auditory brain stem neurons with a low-threshold k current. J Neurophysiol 102(6):3447–3460. https://doi.org/10.1152/jn.00538.2009

Gai Y, Doiron B, Rinzel J (2010) Slope-based stochastic resonance: How noise enables phasic neurons to encode slow signals. PLoS Comput Biol 6:1–15. https://doi.org/10.1371/journal.pcbi.1000825

Goldberg JM, Brown PB (1969) Response of binaural neurons of dog superior olivary complex to dichotic tonal stimuli: some physiological mechanisms of sound localization. J Neurophysiol 32(4):613–636. https://doi.org/10.1152/jn.1969.32.4.613

Golding NL, Oertel D (2012) Synaptic integration in dendrites: exceptional need for speed. J Physiol 590(22):5563–5569. https://doi.org/10.1113/jphysiol.2012.229328

Goldwyn JH, Mc Laughlin M, Verschooten E et al (2017) Signatures of somatic inhibition and dendritic excitation in auditory brainstem field potentials. J Neurosci 37(43):10451–10467. https://doi.org/10.1523/jneurosci.0600-17.2017

Goldwyn JH, Remme MWH, Rinzel J (2019) Soma-axon coupling configurations that enhance neuronal coincidence detection. PLoS Comput Biol 15(3):e1006476. https://doi.org/10.1371/journal.pcbi.1006476

Grau-Serrat V, Carr CE, Simon JZ (2003) Modeling coincidence detection in nucleus laminaris. Biol Cybern 89(5):388–396. https://doi.org/10.1007/s00422-003-0444-4

Grothe B (2003) New roles for synaptic inhibition in sound localization. Nat Rev Neurosci 4(7):540–550. https://doi.org/10.1038/nrn1136

Grothe B, Pecka M, McAlpine D (2010) Mechanisms of sound localization in mammals. Physiol Rev 90(3):983–1012

Grothe B, Leibold C, Pecka M (2018) The medial superior olivary nucleus. https://doi.org/10.1093/oxfordhb/9780190849061.013.9

Huang M, Volgushev M, Wolf F (2012) A small fraction of strongly cooperative sodium channels boosts neuronal encoding of high frequencies. PLoS ONE 7(5):e37,629. https://doi.org/10.1371/journal.pone.0037629

Huguet G, Meng X, Rinzel J (2017) Phasic firing and coincidence detection by subthreshold negative feedback: divisive or subtractive or, better, both. Front Comput Neurosci. https://doi.org/10.3389/fncom.2017.00003

Jeffress LA (1948) A place theory of sound localization. J Comp Physiol Psychol 41(1):35–39. https://doi.org/10.1037/h0061495
Jercog PE, Svirskis G, Kotak VC et al (2010) Asymmetric excitatory synaptic dynamics underlie interaural time difference processing in the auditory system. PLoS Biol 8(6):e1000406. https://doi.org/10.1371/journal.pbio.1000406
Joris PX, Carney LH, Smith PH et al (1994) Enhancement of neural synchronization in the anteroventral cochlear nucleus. I. Responses to tones at the characteristic frequency. J Neurophysiol 71(3):1022–1036. https://doi.org/10.1152/jn.1994.71.3.1022
Kayser C, Logothetis NK, Panzeri S (2010) Millisecond encoding precision of auditory cortex neurons. Proc Natl Acad Sci 107(39):16976–16981. https://doi.org/10.1073/pnas.1012656107
Khurana S, Remme MWH, Rinzel J et al (2011) Dynamic interaction of I_h and I_{K-LVA} during trains of synaptic potentials in principal neurons of the medial superior olive. J Neurosci 31(24):8936–8947. https://doi.org/10.1523/jneurosci.1079-11.2011
Knudsen EI, Konishi M (1979) Mechanisms of sound localization in the barn owl (tyto alba). J Comp Physiol 133(1):13–21. https://doi.org/10.1007/bf00663106
Kuba H (2012) Structural tuning and plasticity of the axon initial segment in auditory neurons. J Physiol 590(22):5571–5579. https://doi.org/10.1113/jphysiol.2012.237305
Kuba H, Ishii TM, Ohmori H (2006) Axonal site of spike initiation enhances auditory coincidence detection. Nature 444(7122):1069–1072. https://doi.org/10.1038/nature05347
Kuba H, Adachi R, Ohmori H (2014) Activity-dependent and activity-independent development of the axon initial segment. J Neurosci 34(9):3443–3453. https://doi.org/10.1523/jneurosci.4357-13.2014
Laback B, Egger K, Majdak P (2015) Perception and coding of interaural time differences with bilateral cochlear implants. Hear Res 322:138–150. https://doi.org/10.1016/j.heares.2014.10.004
Lehnert S, Ford MC, Alexandrova O et al (2014) Action potential generation in an anatomically constrained model of medial superior olive axons. J Neurosci 34(15):5370–5384. https://doi.org/10.1523/jneurosci.4038-13.2014
Lundstrom B, Hong S, Higgs M et al (2008) Two computational regimes of a single-compartment neuron separated by a planar boundary in conductance space. Neural Comput 20:1239–1260. https://doi.org/10.1162/neco.2007.05-07-53
Lundstrom B, Famulare M, Sorensen L et al (2009) Sensitivity of firing rate to input fluctuations depends on time scale separation between fast and slow variables in single neurons. J Comput Neurosci 27:277–290. https://doi.org/10.1007/s10827-009-0142-x
Mathews PJ, Jercog PE, Rinzel J et al (2010) Control of submillisecond synaptic timing in binaural coincidence detectors by kv1 channels. Nat Neurosci 13(5):601–609. https://doi.org/10.1038/nn.2530
Meng X, Huguet G, Rinzel J (2012) Type III excitability, slope sensitivity and coincidence detection. Discrete Contin Dyn Syst Ser A 32(8):2729–2757. https://doi.org/10.3934/dcds.2012.32.2729
Moser T, Neef A, Khimich D (2006) Mechanisms underlying the temporal precision of sound coding at the inner hair cell ribbon synapse. J Physiol 576(1):55–62. https://doi.org/10.1113/jphysiol.2006.114835
Myoga MH, Lehnert S, Leibold C et al (2014) Glycinergic inhibition tunes coincidence detection in the auditory brainstem. Nat Commun. https://doi.org/10.1038/ncomms4790
Pecka M, Brand A, Behrend O et al (2008) Interaural time difference processing in the mammalian medial superior olive: the role of glycinergic inhibition. J Neurosci 28(27):6914–6925. https://doi.org/10.1523/jneurosci.1660-08.2008
Rayleigh L (1907) XII. On our perception of sound direction. Lond Edinb Dublin Philos Mag J Sci 13(74):214–232. https://doi.org/10.1080/14786440709463595
Remme MWH, Donato R, Mikiel-Hunter J et al (2014) Subthreshold resonance properties contribute to the efficient coding of auditory spatial cues. Proc Natl Acad Sci 111(22):E2339–E2348. https://doi.org/10.1073/pnas.1316216111
Reyes A, Rubel E, Spain W (1996) In vitro analysis of optimal stimuli for phase-locking and time-delayed modulation of firing in avian nucleus laminaris neurons. J Neurosci 16(3):993–1007. https://doi.org/10.1523/jneurosci.16-03-00993.1996
Rinzel J, Huguet G (2013) Nonlinear dynamics of neuronal excitability, oscillations, and coincidence detection. Commun Pure Appl Math 66(9):1464–1494. https://doi.org/10.1002/cpa.21469
Roberts MT, Seeman SC, Golding NL (2013) A mechanistic understanding of the role of feedforward inhibition in the mammalian sound localization circuitry. Neuron 78(5):923–935. https://doi.org/10.1016/j.neuron.2013.04.022
Rose HJ, Metherate R (2005) Auditory thalamocortical transmission is reliable and temporally precise. J Neurophysiol 94(3):2019–2030. https://doi.org/10.1152/jn.00860.2004
Scott LL, Hage TA, Golding NL (2007) Weak action potential backpropagation is associated with high-frequency axonal firing capability in principal neurons of the gerbil medial superior olive. J Physiol 583(2):647–661. https://doi.org/10.1113/jphysiol.2007.136366
Sullivan WE, Konishi M (1986) Neural map of interaural phase difference in the owl's brainstem. Proc Natl Acad Sci 83(21):8400–8404. https://doi.org/10.1073/pnas.83.21.8400
Svirskis G, Dodla R, Rinzel J (2003) Subthreshold outward currents enhance temporal integration in auditory neurons. Biol Cybern 89(5):333–340. https://doi.org/10.1007/s00422-003-0438-2
Svirskis G, Kotak V, Sanes DH et al (2004) Sodium along with low-threshold potassium currents enhance coincidence detection of subthreshold noisy signals in mso neurons. J Neurophysiol 91(6):2465–2473. https://doi.org/10.1152/jn.00717.2003
Tollin D, Yin T (2009) Sound localization: neural mechanisms. In: Encyclopedia of neuroscience. Elsevier, pp 137–144, https://doi.org/10.1016/b978-008045046-9.00267-9
von Campenhausen M, Wagner H (2006) Influence of the facial ruff on the sound-receiving characteristics of the barn owl's ears. J Comp Physiol A 192(10):1073–1082. https://doi.org/10.1007/s00359-006-0139-0
Winters BD, Jin SX, Ledford KR et al (2017) Amplitude normalization of dendritic EPSPs at the soma of binaural coincidence detector neurons of the medial superior olive. J Neurosci 37(12):3138–3149. https://doi.org/10.1523/jneurosci.3110-16.2017
Winters BD, Golding NL (2018) Glycinergic inhibitory plasticity in binaural neurons is cumulative and gated by developmental changes in action potential backpropagation. Neuron 98(1):166-178.e2. https://doi.org/10.1016/j.neuron.2018.03.001
Yin TC, Chan JC (1990) Interaural time sensitivity in medial superior olive of cat. J Neurophysiol 64(2):465–488. https://doi.org/10.1152/jn.1990.64.2.465